















## RESEARCH ARTICLE

10.1029/2019JE006262

## Chandra Observations of Jupiter's X-ray Auroral Emission During Juno Apojove 2017

## Special Section:

Jupiter Midway Through the Juno Mission

D. M. Weigt<sup>1</sup> , C. M. Jackman<sup>1,2</sup> , W. R. Dunn<sup>3,4,5</sup> , G. R. Gladstone<sup>6,7</sup> , M. F. Vogt<sup>8</sup> ,  
A. D. Wibisono<sup>3,4</sup> , G. Branduardi-Raymont<sup>3,4</sup> , D. Altamirano<sup>1</sup>, F. Allegrini<sup>6,7</sup> ,  
R. W. Ebert<sup>6,7</sup> , P. W. Valek<sup>6</sup> , M. F. Thomsen<sup>9</sup> , G. Clark<sup>1,10</sup> , and R. P. Kraft<sup>5</sup>

## Key Points:

- Analysis is performed on a Chandra campaign observing Jupiter's X-ray emissions during the apojove portion of Juno's orbit on 18 June 2017
- We use Juno magnetopause crossings to infer a compressed magnetosphere during the X-ray campaign
- Quasiperiodic pulsing of the northern X-ray hot spot are mapped to a location close to the dayside magnetopause

## Correspondence to:

D. M. Weigt,  
D.M.Weigt@soton.ac.uk

## Citation:

Weigt, D. M., Jackman, C. M., Dunn, W. R., Gladstone, G. R., Vogt, M. F., Wibisono, A. D., et al. (2020). Chandra observations of Jupiter's X-ray auroral emission during Juno apojove 2017. *Journal of Geophysical Research: Planets*, 125, e2019JE006262. <https://doi.org/10.1029/2019JE006262>

Received 30 OCT 2019

Accepted 24 FEB 2020

<sup>1</sup>School of Physics and Astronomy, University of Southampton, Southampton, UK, <sup>2</sup>Astronomy and Astrophysics Section, Dublin Institute for Advanced Studies, Dublin, Ireland, <sup>3</sup>Mullard Space Science Laboratory, Department of Space and Climate Physics, University College London, Dorking, UK, <sup>4</sup>The Centre for Planetary Science at UCL/Birkbeck, London, UK, <sup>5</sup>Harvard-Smithsonian Center for Astrophysics, Smithsonian Astrophysical Observatory, Cambridge, MA, USA, <sup>6</sup>Space Science and Engineering Division, Southwest Research Institute, San Antonio, TX, USA, <sup>7</sup>Department of Physics and Astronomy, University of Texas at San Antonio, San Antonio, TX, USA, <sup>8</sup>Center for Space Physics, Boston University, Boston, MA, USA, <sup>9</sup>Planetary Science Institute, Tucson, AZ, USA, <sup>10</sup>Johns Hopkins University Applied Physics Laboratory, Laurel, MD, USA

**Abstract** Jupiter's auroral X-rays have been observed for 40 years with an unknown driver producing quasiperiodic emission, concentrated into auroral hot spots. In this study we analyze an ~10-hr Chandra observation from 18:56 on 18 June 2017. We use a new Python pipeline to analyze the auroral morphology, perform timing analysis by incorporating Rayleigh testing, and use in situ Juno observations to infer the magnetosphere that was compressed during the Chandra interval. During this time Juno was near its apojove position of ~112  $R_J$ , on the dawn flank of the magnetosphere near the nominal magnetopause position. We present new dynamical polar plots showing an extended X-ray hot spot in the northern auroral region traversing across the Jovian disk. From this morphology, we propose setting a numerical threshold of >7 photons per 5° System III longitude × 5° latitude to define a photon concentration of the northern hot spot region. Our timing analysis finds two significant quasiperiodic oscillations (QPOs) of ~37 and ~26 min within the extended northern hot spot. No statistically significant QPOs were found in the southern X-ray auroral emission. The Rayleigh test is combined with Monte Carlo simulation to find the statistical significance of any QPOs found. We use a flux equivalence mapping model to trace the possible origin of the QPOs, and thus the driver, to the dayside magnetopause boundary.

## 1. Introduction

The year 2019 marked 40 years since the first observation of Jupiter's auroral X-rays by the Einstein Observatory (Metzger et al., 1983). Since then, with the high spatial resolution of Chandra (Weisskopf et al., 2000) and high spectral resolution of XMM-Newton (Jansen et al., 2001), we now know that there are two components of X-ray emission on Jupiter: disk emission and the auroral emission originally found by the Einstein Observatory. The disk emission has been observed to be a result of fluorescence and elastic scattering of solar X-rays and has been found to follow the solar cycle (Bhardwaj et al., 2005; Branduardi-Raymont et al., 2004, 2007a; Elsner et al., 2005; Maurellis et al., 2000). The auroral emission can be further split into two constituents: hard X-rays (HXR, photon energy >2 keV) and soft X-rays (SXR, photon energy <2 keV) (Branduardi-Raymont et al., 2008). The HXR from Jupiter are found to overlap the ultraviolet (UV) main oval and are a result of X-ray bremsstrahlung. The SXR are observed at higher latitudes than the HXR and are thought to be a result of charge exchange processes between precipitating ions and neutrals in the Jovian atmosphere (Bhardwaj & Gladstone, 2000; Cravens et al., 1995). The heavy ion precipitation can occur on open field lines connected to the solar wind or on closed field lines mapping to the outer magnetosphere (Cravens et al., 2003). For this process to occur within the Jovian system, field-aligned electric fields, producing potentials of ~200 kV to 8 MV must exist between the ionosphere and the magnetosphere.

This emission is found to mainly reside in a "hot spot" of emission near the northern and southern poles with a total power of 1 GW to a few GW. Recent work, using the most updated Jovian ion models and in situ data, has found that the very energetic heavy ions (up to approximately few MeV and above in some cases)

©2020. The Authors.

This is an open access article under the terms of the Creative Commons Attribution License, which permits use, distribution and reproduction in any medium, provided the original work is properly cited.

in this region are responsible for most of the total power output of the X-rays (Houston et al., 2019). The X-ray emissions in this region have been observed to exhibit quasiperiodic pulsations during several intervals (Dunn et al., 2016, 2017; Elsner et al., 2005; Gladstone et al., 2002; Jackman et al., 2018; Kimura et al., 2016). There have been very few observations of the southern aurora due to the geometry of the emission and the tilt of the planet making for unfavorable viewing conditions. Ozak et al. (2010) found from their modeling of sulfur and oxygen ion precipitation at high latitudes fitted to observations that the opacity of the Jovian atmosphere can inhibit the outgoing X-rays. Therefore, a highly opaque atmosphere coupled with poor viewing geometry will drastically reduce the intensity of the X-rays observed.

The true origin of the SXR and where they map to in the magnetosphere are also under debate. Previous studies have found X-ray observations where internally driven processes dominate the production of the X-rays (detections of  $S^+$ ,  $O^+$ , and  $O^{++}$  from Io flux tubes) and times where the solar wind ions dominate (detections of lighter ions such as carbon) (Branduardi-Raymont et al., 2007a, 2007b; Dunn et al., 2016; Elsner et al., 2005; Hui et al., 2010; Kimura et al., 2016). Most of these studies were pre-Juno and relied on propagated solar wind parameters from models to attempt to infer the driver. Why the hot spot pulsations vary over a Jupiter rotation and are different study to study (Jackman et al., 2018) and the changing morphology of the aurora are still unanswered questions in the field. Now with Juno in situ auroral high-energy electron and ion data in concert with X-ray observations, the source of SXRs, and therefore the variations we observe, may be found. The unique polar orbit of Juno (Bolton et al., 2017) can allow many different processes to be explored to try and fully understand the solar wind-ionosphere-magnetosphere coupling at Jupiter. At perijove Juno is closest to the planet in its orbit and the many processes that produce the aurora, storms, and other phenomena at the poles can be explored in detail as Juno directly traverses the magnetic field lines along which auroral currents flow. At apojove in the early part of the mission, Juno is near the nominal magnetopause position on the dawn flank, which can allow possible auroral drivers like Kelvin-Helmholtz instability (KHI), magnetopause reconnection (Ebert, Allegrini, Bagenal, Bolton, Connerney, Clark, DiBraccio, et al., 2017), and possible cusp reconnection (depending on the local time (LT) of Juno) (Bunce et al., 2004) to be explored. Data from the Jovian Auroral Distributions Experiment (JADE) (McComas et al., 2017) and the Jupiter Energetic Particle Detector Instrument (JEDI) (Mauk et al., 2017) on board Juno allow magnetopause crossings to be found (Ebert, Allegrini, Bagenal, Bolton, Connerney, Clark, DiBraccio, et al., 2017; Mauk et al., 2019; McComas et al., 2017) and can be used in association with the Joy et al. (2002) model to infer a dynamic pressure of the magnetosphere during the observation.

The high spatial resolution of Chandra combined with the time-tagged nature of the X-ray photon data enables us to spatially select hot spots and study any quasiperiodic oscillations (QPOs) in the X-ray emission. The first observation and study of the northern hot spot conducted by Gladstone et al. (2002) found a QPO at  $\sim 45$  min. Prior to the Gladstone et al. (2002) X-ray study, QPOs were found from Jovian radio emissions. A Ulysses flyby of Jupiter found 40-min oscillations originating from high-energy particles in the outer magnetosphere and radio waves (Krimigis et al., 2002; MacDowall et al., 1993). Intermittent bursts of 1–200 kHz of radio emissions with a period of  $\sim 40$  min were observed for several months at high southern Jovian latitudes following the Ulysses flyby (MacDowall et al., 1993). Gladstone et al. (2002) suggested the similar periodicities found from the X-ray, and radio data may show that X-ray auroral emission results from unexplained processes in the outer magnetosphere, producing highly variable emission. Bunce et al. (2004) suggested that intermittent bursts with period of 40–50 min may be explained by cusp reconnection. They show using this model that this process would be able to produce the approximately few GW of total power in the X-ray emissions observed. However, subsequent studies did not find the  $\sim 45$ -min period reported by Gladstone et al. (2002) to be a regular feature of the X-ray data. Rather, a large statistical study by Jackman et al. (2018) found that statistically significant QPOs are relatively rare in the Jovian X-ray data, and where present, periods can differ from observation to observation and can change on timescales less than a Jovian rotation. Dunn et al. (2017) found that the north and south hot spots are nonconjugate and can pulsate independently from each other. This was one of the first observations where the viewing geometry favored both the north and south poles.

Chandra's spatial resolution also allows us to map the X-ray photons reregistering the brighter pulsating hot spot to its location within the Jovian ionosphere. The flux equivalence mapping model by Vogt et al. (2011, 2015) allows the hot spot, and in turn the QPOs, to be mapped to their origin within the magnetosphere, returning a LT and radial distance (within uncertainties) at which X-ray-producing currents are thought to originate. Previous mapping attempts by Kimura et al. (2016) and (Dunn et al., 2016, 2017) used

the VIPAL (Hess et al., 2011) and Grodent Anomaly (Grodent et al., 2008) field models, respectively, with the (Vogt et al., 2011, 2015) flux equivalence model. In this paper, we update this mapping with the most recent JRM09 magnetic model, which utilizes the Juno magnetometer data to improve upon previous models (Connerney et al., 2018). The mapping techniques from both Chandra and the magnetospheric mapping model allow us to try and constrain the origin of the X-rays found in Jupiter's pulsating hot spot.

In section 2 below we discuss the data sets used for this study and the new Python pipeline used to analyze the Chandra data obtained. Section 3 discusses the morphology of the X-ray emissions, the definition of the hot spot, and the timing analysis of the pulsating emissions. Furthermore, the X-rays are mapped using the flux equivalence mapping model by Vogt et al. (2011, 2015) with the latest JRM09 magnetic field model (Connerney et al., 2018) to attempt to isolate the location of their source. Section 4 contains a discussion and interpretation of the results.

## 2. Data Sets and Processing Methods

The data used in this study are from the high-resolution camera (HRC-I) on board the Chandra X-ray Observatory and in situ data from JADE and JEDI on the Juno spacecraft. Chandra observed on 18 June 2017 for  $\sim 10$  hr ( $\sim 1$  Jupiter rotation) when Juno was close to apojove at  $\sim 111 R_J$  on the dawn flank, close to the nominal location of Jupiter's magnetopause. An XMM-Newton observation lasting  $\sim 24$  hr in total and overlapped with the final 5 hr of the Chandra observation. Recent findings from this study are in Wibisono et al. (Temporal and spectral studies by XMM-Newton of Jupiter's X-ray aurorae during a compression event, submitted to *J. Geophys. Res.*, 2019, in review at the time of writing, herein referred to as Wibisono et al., (submitted, 2019)). The Hubble Space Telescope and the Nuclear Spectroscopic Telescope Array also observed Jupiter during this time taking full advantage of Juno's apojove position.

### 2.1. Chandra

The Chandra HRC-I incorporates a single large-format microchannel plate and allows high spatial resolution of  $\sim 0.4$  arcsec over a  $30$  arcmin  $\times$   $30$  arcmin field of view (Weisskopf et al., 2000). The aim point is at the center of the field of view, where the best image quality is found. The instrument can detect photons with energies between 0.08 and 10 keV. Chandra HRC does not provide energy resolution so it is not possible to identify the average energy of the precipitating photons. However, based on previous studies with Chandra ACIS (Branduardi-Raymont et al., 2008; Elsner et al., 2005) and XMM-Newton (Branduardi-Raymont et al., 2004, 2007b), the aurora is typically dominated by SXR spectral line emission from 0.2–0.9 keV, with a bremsstrahlung continuum component up to several keV. Typically, this emission has two broad peaks, one below 0.4 keV associated with sulfur or carbon ions and one between 0.5 and 0.8 keV associated with oxygen ions. During the June 2017 campaign, the HRC-I instrument pointed at Jupiter and traced the planet's motion across the sky. As a result, the full image taken by HRC-I appears as multiple streaks of Jovian X-ray emission due to the fast motion of Jupiter across the detector. This can be corrected for as the data are time tagged, and the photon positions can be traced back to their origin on the disk. We use methods in Gladstone et al. (2002) and Elsner et al. (2005) translated into Python to perform this correction on the Chandra data. The X-rays can then be mapped using the Gaussian point spread function (PSF) of the instrument and a coordinate transformation into Jovian System III (S3) coordinates. This shows the position and morphology of the Jovian X-ray aurora. The assumptions used for the mapping assume that the FWHM of the HRC PSF is 0.8 arcsec. with a PSF size of 25 arcsec. The altitude at which X-ray emission occurs is assumed to be 400 km above the 1-bar atmosphere for the mapping pipeline. The scaling used for the maps is 0.13175 arcsec per pixel.

### 2.2. Juno JADE and JEDI

The in situ data from Juno JADE and JEDI are used to provide magnetospheric context for the Chandra observations over an  $\sim 5$ -day interval bracketing the 10-hr Chandra observation. JADE provides measurements of the electrons and ions via two separate sensors. JADE-I (a single ion sensor) can measure ions from  $\sim 5$  eV to  $\sim 50$  keV over a  $270^\circ \times 90^\circ$  field of view in 2 s over all directions in each 30-s rotation of Juno (McComas et al., 2017). JADE-I can also separate heavy and light ions in the Jovian magnetosphere. JADE-E (two electron sensors) is separated  $120^\circ$  apart around Juno to measure electron distributions from  $\sim 0.1$  to  $\sim 100$  keV. The ion and electron measurements allow us to determine when Juno crosses the magnetopause.

JEDI measures the energetic electrons and ions that (a) are a key component to the production of the aurora on Jupiter, (b) are found to heat and ionize the upper atmosphere of Jupiter, and (c) provide signatures of the

Chandra X-ray Jupiter Polar Maps - ObsID 20001 (July 18 18:56 - July 19 05:15)

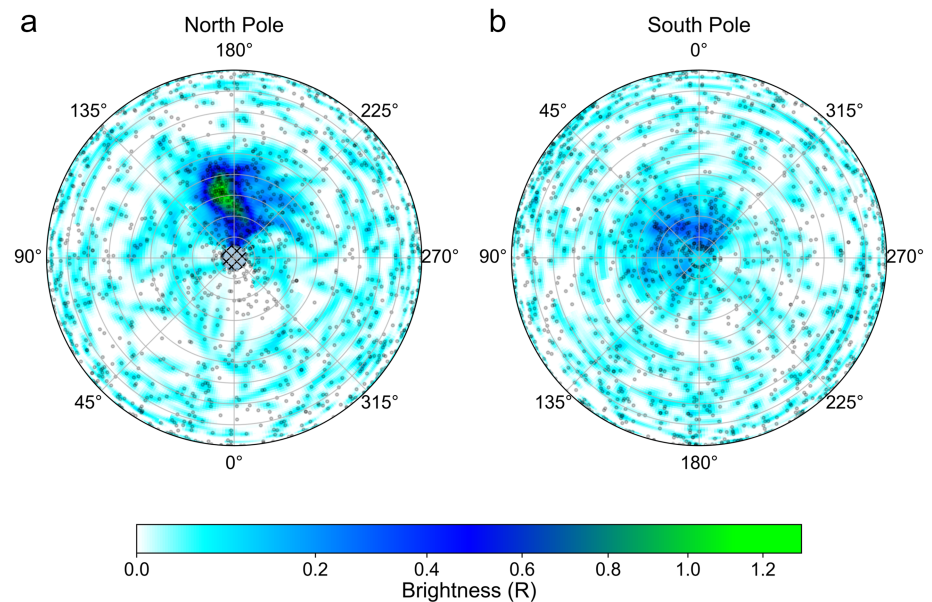


**Figure 1.** Polar plots of (a) Jupiter's north and (b) south poles as viewed from above. The azimuth angle (in jovigraphic longitude) within the polar plot (in degrees) is indicated around the plot. The concentric circles represent  $10^\circ$  latitude increments. Semitransparent black dots indicate the location of individual X-ray photons as detected by the Chandra-HRC instrument. The brightness of the X-ray emissions is proportional to the photon flux (calculated from the point spread function (PSF)) and is denoted by the color bar below in units of Rayleighs (R). The PSF shows the number density of photons detected with an uncertainty on its position (spreading of the PSF). The regions which have little to no X-ray emissions are represented in white. Regions out of Chandra's field of view are denoted by the cross-hatched area. Photons over plotted onto regions of no X-ray emission may be a consequence of photons detected on the limb of Jupiter. Combined with increasing spatial uncertainty (as the photons are detected away from the centre of the detector), the positions of limb photons are difficult to trace back accurately.

structure of Jupiter's magnetosphere, focusing mainly on particles belonging to the inner magnetosphere (Mauk et al., 2017). JEDI makes measurements of the energy, pitch angle, and ion composition distributions of ions from 20 keV (H) and 50 keV (heavier O) to energies  $>1$  MeV. The energies of electrons,  $E$ , detected by JEDI are between  $E < 40$  to  $E > 500$  keV. The time of flight and pulse height of incoming ions are measured using microchannel plates and thin foils. The total energies of both ions and electrons are measured using solid state detectors.

### 3. Results

#### 3.1. Auroral X-ray Morphology

Polar plots of the X-rays detected by Chandra during the interval enable us to examine the morphology of the auroral X-rays in detail, using the pipeline discussed in section 2.1. This also allows the properties of the hot spot to be explored and analyzed in greater detail. Figure 1 shows (a) the north and (b) south pole, as viewed from above the pole, over an interval of  $\sim 10$  hr from 18:56 on 18 June 2017 to 19 June 2017 05:15. A total of 2,883 photons is detected throughout the observation from Jupiter with 342 photons from the north pole and 180 from the south selected from a region using SAOImageDS9 and spatially select regions of the concentrated X-ray emissions. Assuming a photon energy of  $\sim 0.5$  keV (halfway between the sulfur and oxygen emission lines), the power of the north and south auroral emissions was found to be  $\sim 2.6$  and  $0.7$  GW, respectively. The remainder of the photons originate from the disk and are not the focus of this study. In agreement with previous studies, the northern X-ray auroral region is observed to be more intense than the southern (Dunn et al., 2017; Jackman et al., 2018). In previous literature, most of the auroral X-ray emission was found concentrated into a "hot spot" (Branduardi-Raymont et al., 2004, 2008; Dunn et al., 2016, 2017; Gladstone et al., 2002). The X-ray emission from the hot spot during this observation however is found to be more extended in the north and is observed from  $\sim 160$ – $190^\circ$  S3 longitude and  $\sim 57$ – $76^\circ$  latitude using a numerical threshold. This differs slightly from previous studies where the locations of the hot spot were

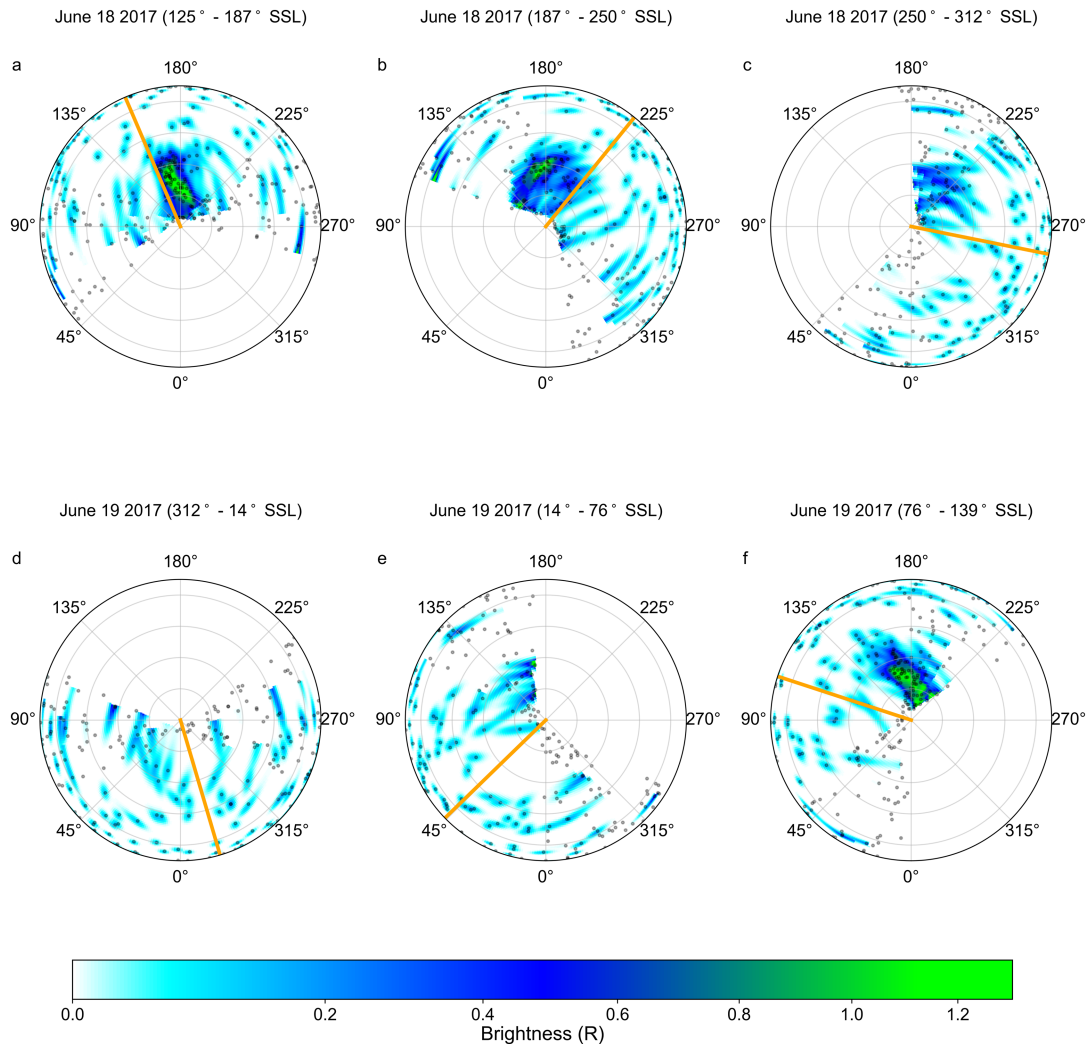


**Figure 2.** (a–f) The full ~10-hr observation of the north pole split into six equal ~60° subsolar longitude (SSL) intervals (each corresponding to ~100 min of the observation), in a similar format to Figure 1a. The orange line indicates the SSL midway through the interval. The concentric circles represent 20° latitude increments. The north hot spot is observed in intervals (a), (b), and (f).

determined by eye (Gladstone et al. (2002) ~–180° S3 longitude, ~57–76° latitude and (Dunn et al., 2017) ~155–180° S3 longitude, ~60–75° latitude).

During this interval the northern and diffuse southern X-ray hot spots are found to traverse the face of the Jovian disk. This results from the rotation of the planet, and the SXR from the hot spot are found to be concentrated in a particular jovigraphic longitude region. The highest concentrations of X-ray are found in the hot spot regions (the darker blue to bright green regions on the polar plots). Figure 2 shows the morphology of the X-ray emission of the north pole over the full Chandra observation split into six ~60° SSL intervals (each having a duration of ~100 min). The brighter X-ray region appears in the Chandra observations as shown in Figures 2a, 2b, and 2f. Each of these intervals also shows the presence of the extended hot spot emission from the northern hot spot (as shown in Figure 1a). As expected, when the hot spot is in view, the majority of the photons detected are found in this region. The blank white spaces on both Figures 2 and 5 illustrate the regions where little to no X-ray emission was observed during this interval. The brightness from the PSF in Figures 2 and 5 appears as streaks on the polar plot from the motion of Chandra itself as it observes Jupiter at different central meridian longitudes (CML). This streaking is further enhanced by the polar coordinate transformation of the PSF wrapped around Jupiter itself. This effect is more predominant in the X-ray emission detected away from the aim point. Using the subobserver longitude from Earth to Jupiter (from JPL Horizons <https://ssd.jpl.nasa.gov/>) and the location of hot spot found from

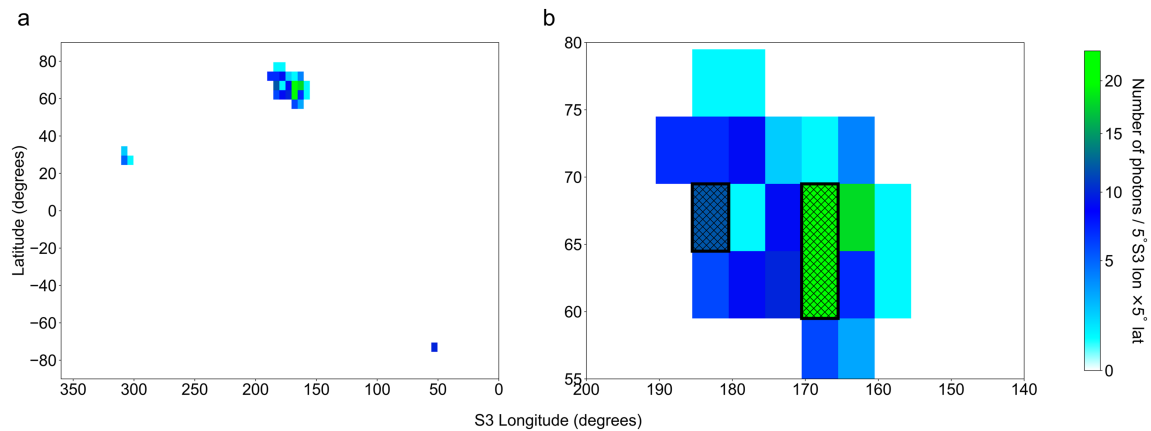


**Figure 3.** Plots of S3 longitude versus latitude showing the position and number of photons per (a)  $5^\circ$  S3 lon  $\times$   $5^\circ$  lat of the full map and (b)  $5^\circ$  S3 lon  $\times$   $5^\circ$  lat of the northern X-ray region during the full Chandra observation. The threshold used for selecting the brighter X-ray emission is an area of  $5^\circ \times 5^\circ$  with  $>7$  photons, using the HRC-I instrument, within this area and lying on the boundary. The numbers of photons within the region defined are plotted using a 2-D histogram to remove the effect of double counting. The colors here represent the number of photons within the region of X-ray emission defined by the threshold. Panel (b) shows that the northern hot spot (depicted by the darker blue and green regions) is more extended than what was observed in previous studies (Dunn et al., 2017; Gladstone et al., 2002). The centers of two possible independent X-ray sources are denoted by black cross-hatched rectangles.

Figures 1a and 2, the northern extended hot spot is expected to be in view with a CML of  $60\text{--}290^\circ$  ( $\pm 90^\circ$  to the S3 longitude of the hot spot). The time at which this CML range occurs during the Chandra observation is found from JPL Horizons and is then compared to the intervals shown in Figure 2. We therefore find that the hot spot should traverse the disk over a period of  $\sim 320$  min.

Based on examination of the spread of photons in Figure 1a, we propose setting a threshold of  $>7$  photons per  $5^\circ$  S3 lon  $\times$   $5^\circ$  lat to define the concentration of the hot spot. The photons that are found to lie within this area and on the boundaries are counted (Figure 3). This threshold is determined from counting the number of photons within the concentrated X-ray hot spot from previous studies (Chandra observations previously analyzed by Gladstone et al., 2002; Dunn et al., 2016, 2017) over a selected range of S3 longitudes and latitudes. The position and density of the photons observed within a  $1^\circ$  S3 lon  $\times$   $1^\circ$  lat region from the threshold are also plotted (Figure 4). This allows the number of photons to be found at a higher resolution

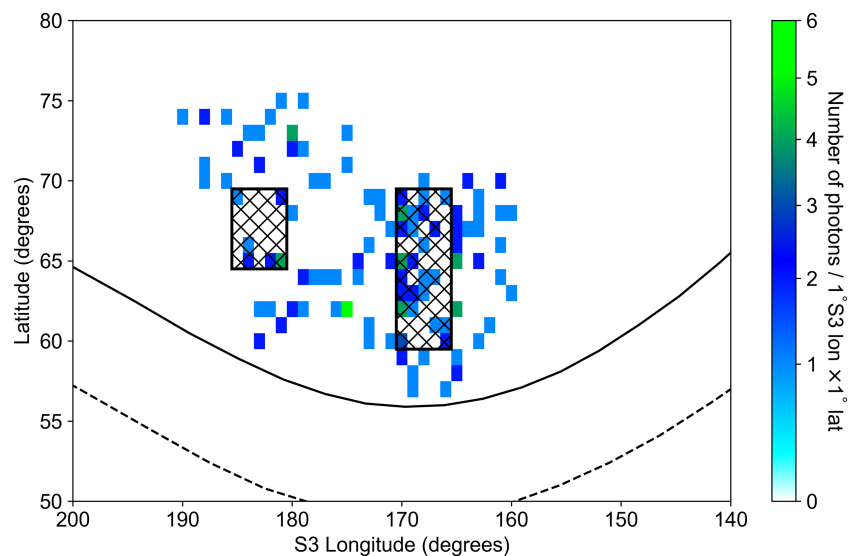


**Figure 4.** Similar format to Figure 3 except showing the position and number of photons per  $1^\circ$  S3 lon  $\times$   $1^\circ$  of the northern X-ray region. The position of the Io footprint (black dashed line) and main auroral oval (black solid line) are plotted to provide context to the hot spot location (Grodent et al., 2008). The photon density plot shows the position of the photons detected by Chandra. The same threshold defined previously is used for selecting the northern X-ray region. The extended hot spot as depicted in Figures 1 and 3 is still present when using a higher spatial resolution.

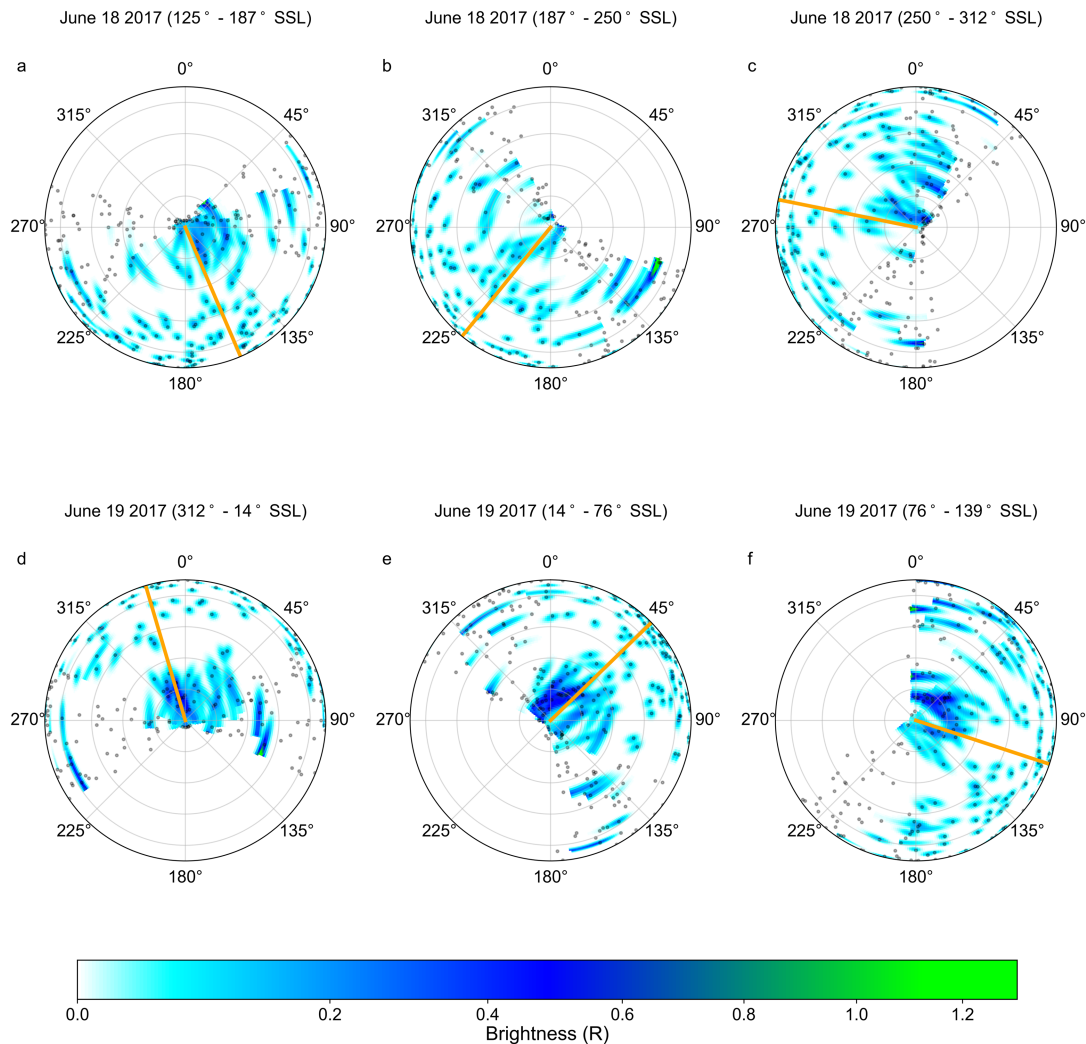


**Figure 5.** (a–f) The full ~10 hr observation of the south pole split into six equal SSL intervals, in the same format as Figure 6. The more diffuse south “hot spot” is observed in intervals (d), (e), and (f).

and allows the finer structures within the hot spot region to be explored in more detail. The numerical threshold also confirms the position and morphology of the extended hot spot as shown in Figure 1a). The effect of double counting from the photons lying on the boundary of the areas counted is removed by plotting the positions using a 2-D histogram as shown in Figures 3 and 4. It is clear that, although the X-ray region seems to appear in approximately the same location as found from previous studies, the morphology of the emitting region does not always resemble that of a concentrated “spot” of emission. The hot spot we observe in this study may host two possible independent X-ray sources as there are two regions within the hot spot of a high density of photons separated by a low density boundary. The centers of the two possible regions are highlighted in Figures 3 and 4 by a black cross-hatched rectangle. The peak concentration of the brighter X-ray source is 23 photons per  $5^\circ$  S3 lon  $\times$   $5^\circ$  lat with the center of the second source having a peak concentration of 12 photons per  $5^\circ$  S3 lon  $\times$   $5^\circ$  lat. Therefore, an extended region of X-ray emission may be a result of multiple processes.

Figure 5 shows the morphology of the X-ray emission of the south pole over the full Chandra observation, over the same time intervals as Figure 2. The southern X-ray emission during this time is observed to be more diffuse and less intense than the north, resulting in no definitive “hot spot” observed by Chandra during this interval. Therefore, an exact position (in S3 lon, lat) of the hot spot could not be determined in this study. The difference in intensity indicates that the north and south X-ray emission may originate from different locations and/or created by different mechanisms as found by previous studies (Dunn et al., 2017; Jackman

et al., 2018). From the recent JRM09 magnetic field model by Connerney et al. (2018), the magnetic field in the south is found to be weaker than the field in the North. This may also contribute to the asymmetry in intensity. The brighter component of the diffuse hot spot detected by Chandra is shown in Figures 5d–5f.

### 3.2. Rayleigh Test Results

With the location and morphology of the hot spot found, we use timing analysis to quantify any statistically significant periodic emission in the X-rays. As mentioned in section 3.1, during the ~10-hr interval of Chandra observation on 18/19 June, the extended north hot spot came into view twice: once at the beginning (0 to 210 min—North HS1) and again at the end of the observation window (500 to 620 min—North HS2). This is shown clearly from the light curve of the full observation in Figure 6a where flaring of the X-rays is detected by Chandra. These two intervals, of 210 and 120 min, respectively, are shown in Figures 6d–6f and Figures 6g–6i. During these time intervals, we use a spatial downselect of S3 longitude 150–200° and latitude 55–80° to isolate the photons that are associated with the extended hot spot region (Figures 3 and 4).

Figures 6a, 6d, and 6g show the light curve of X-ray photons from the north polar region with 60-s binning applied. The binning used for the light curve is purely for presentation purposes and not used in the timing analysis. The quantized nature of the X-ray emission is shown clearly in the light curves with many time bins containing no photons at all. The periods where these 0 values occur are true nondetections made by Chandra and are not gaps in the data set as discussed by Jackman et al. (2018).

To account for the low photon count detected by Chandra, we use a Rayleigh test to perform our timing analysis on the X-ray emissions and look for periodicities in the light curve. In order to use this statistical analysis, the data must be unbinned and may be irregularly sampled such as the time-tagged photons detected by Chandra during this time (Brazier, 1994). We believe that this method is superior to fast Fourier transforms and Lomb-Scargle analysis used elsewhere in the field because it does not require any binning of the data (which can result in missing shorter periods) and is particularly suitable for a sparse count regime. The test associates each time-tagged photon with the phase for each assumed frequency and then searches to see whether the distribution of phases is uniform (no period detected) or whether there are local anomalies (significant (quasi)period detected). It then returns a power spectrum. The statistical power from the test is highest for smooth, quasi-sinusoidal signals and the harmonics of the fundamental frequency of sharp pulsed signals (Jackman et al., 2018). The statistical significance of any quasiperiodic signals found can be evaluated when combined with Monte Carlo simulations. This allows us to estimate the likelihood of finding a maximum peak as observed from the Chandra light curves under the null hypothesis (no periodic signal). The Monte Carlo simulations consist of randomly shuffled fake light curves over the same time interval as the real Chandra data. The same Rayleigh analysis is performed on each light curve using an identical frequency grid. This is carried out for 10,000 different shuffled combinations. The Monte Carlo simulations take into account the fact that we inspect many frequencies when searching for a statistically significant (quasi)periodic signal. Figures 6b, 6c, 6e, 6f, 6h, and 6i show the results of the Rayleigh analysis with the Monte Carlo simulations. The timing analysis and significance testing methods employed here (tailored to Chandra data) are outlined in detail in Jackman et al. (2018).

Figures 6b, 6e, and 6h show a periodogram of the Rayleigh power versus period. The best quasiperiod from the light curves and their associated power is indicated by a blue dashed vertical line. The frequency grid used for the periodogram consists of 150 logarithmically spaced out frequencies and corresponds to a period range between 2 and 100 min. From the viewing window of the Chandra observation and based on the results of previous large statistical surveys (e.g., Jackman et al., 2018), we might expect to find frequencies corresponding to periods of ~8 to ~46 min. The logarithmic frequency grid we use in this study ensures that any peaks found in this range will be well defined.

Figures 6c, 6f, and 6i show histograms of the maximum Rayleigh power found from each of the 10,000 Monte Carlo simulations as a Poisson distribution. The corresponding power from the most significant period is plotted as a vertical dashed blue line. The red curve overlaid on the histograms demonstrates the cumulative distribution of the histograms. The position of the dashed blue line with respect to the red cumulative distribution curve in these panels shows where the highest power from the Chandra input data would lie on any random distribution of photons. The 99th percentile of the 10,000 Monte Carlo simulations is depicted as a horizontal black dashed line in the figures. Any quasiperiods detected above the 99th percentile are considered to be significant. When there are multiple peaks above this 99th percentile (as demonstrated in Figures 6b), the peak with the highest Rayleigh power is considered the best period for the interval.



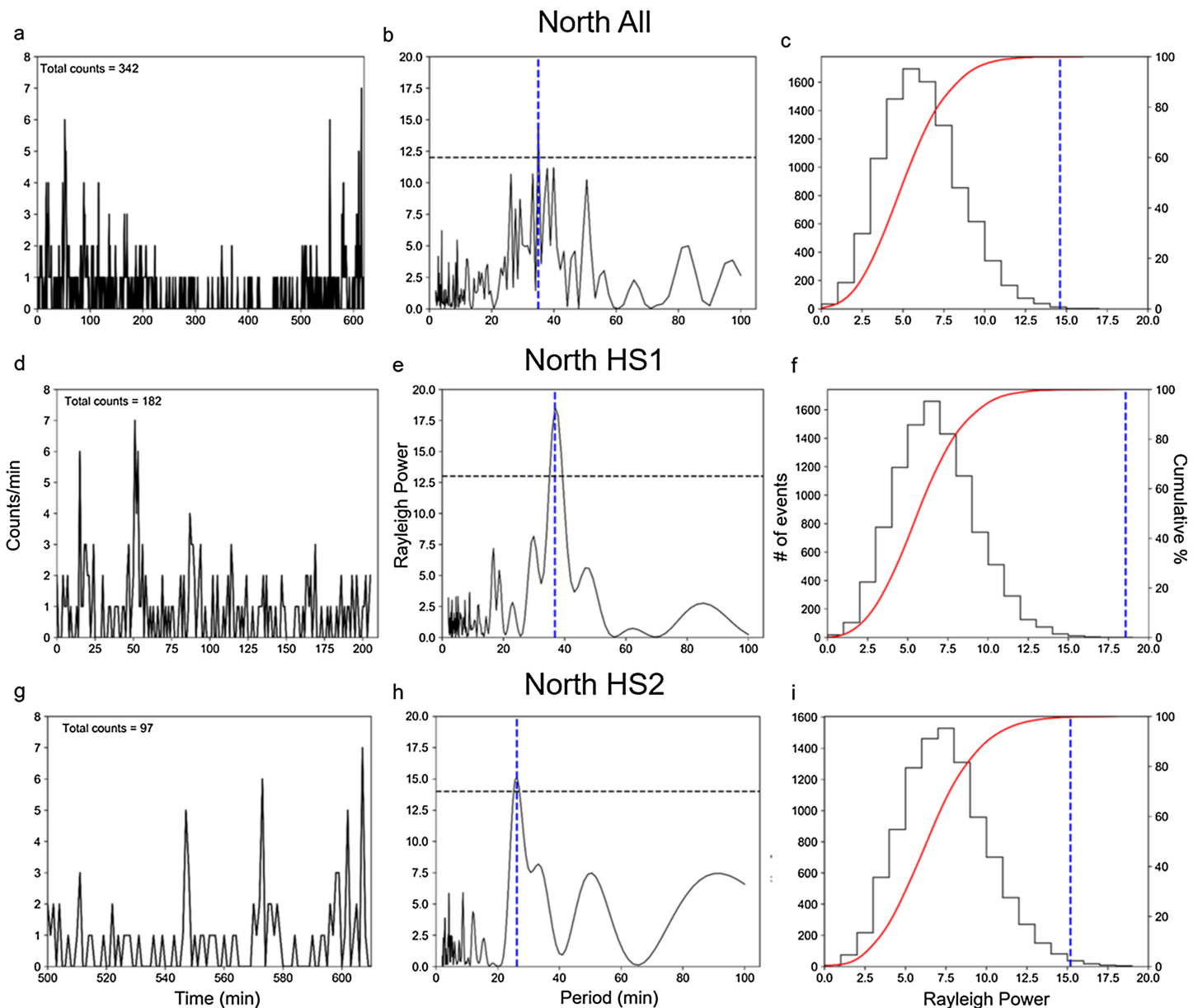


**Figure 6.** Results from the Rayleigh test performed on the full light curve (a) to (c), the first time the extended hot spot is in view (North HS1—(d) to (f)), and when it reappeared at the end of the observation window (North HS2—(g) to (i)). Figures 6a, 6d, and 6g show a light curve of time tagged photons in the northern region of Jupiter from the full observation, 0 to 210 and 500 to 620 min, respectively. The photons are binned into 60 s bins, and the data have not been smoothed. Figures 6b, 6e, and 6h show a periodogram (power versus period) from the Rayleigh test on the input light curve for each interval. The peak power corresponding to the best quasiperiod is indicated by a vertical dashed blue line and the 99th percentile of the power from the 10,000 Monte Carlo simulations by a horizontal black dashed line. The best periods are found to be ~35 min for the full light curve, ~37 min for HS1 and ~26 min for HS2. Figures 6c, 6f, and 6i show a histogram of the maximum powers from the Rayleigh analysis of 10,000 light curves based on the original input data, randomly shuffled. The corresponding peak power from the best quasiperiod is again represented by the vertical dashed blue line. The red line indicates the cumulative probability distribution of the maximum powers found from the Rayleigh test. The analysis performed used an identical Rayleigh test for each region of the light curve.

From the Rayleigh test results of the full light curve (Figures 6a–6c), we find a quasiperiod of ~35 min with a significance of 99.94% ( $p$  value 0.0006 or 6 out of 10,000 results from test greater than peak power). The light curve (Figure 6a) shows that there are pulses from the full light curve at the beginning of the observation window and again at the end. Figure 6b shows that there are multiple peaks in the periodogram above the 99th percentile line, indicating the possibility of quasi-pulsations within the signal. From the signal found from the full light curve, we further investigate the beginning (North HS1) and end (North HS2) of the observation window to try and find significant quasiperiods using the Rayleigh test.

Figures 6d–6f show the light curve and Rayleigh test results of the first 210 min of the Chandra observation. The periodogram (Figure 6e) shows that a best period of  $\sim 37$  min is found from the North HS1 light curve. The period had a significance of 99.98% ( $p$  value 0.0002 or 2 out of 10,000 results from test greater than peak power) and is the only peak above the threshold. Figures 6g–6i show the light curve and Rayleigh analysis for the final 120 min of the observation. The periodogram (Figure 6h) shows that we find a best period of  $\sim 26$  min during this interval, and this is the only period above the threshold. The highest power from both intervals of the Chandra input data is far above what we would typically expect from analyzing any random distribution of photons (as shown in Figures 6f and 6i). Therefore, for this Chandra observation, we find two significant best periods for QPOs over a timescale less than a Jupiter rotation. Jackman et al. (2018) found from their large statistical heritage study that only one other Chandra observation ( $\sim 11$  hr observation from 08:18, 8 April 2014) had two significant QPOs using the Rayleigh test. The pulsations from the April 2014 observation were found in the southern hot spot as opposed to the north.

The multiple significant periods we find in this study may be a result of multiple processes within the elongated hot spot itself as well as changing magnetospheric conditions where the X-rays originate from. We note that the significances calculated for both QPOs using the Rayleigh test do not take into account the red noise found in the light curve. Red noise is a type of signal noise produced by the random motion of particles in a medium, resulting from collisions with faster moving particles in the same medium. Any process that produces time series in which the periodogram has a significant power that can be described by a power law index  $> 0$  is known as colored noise. In the literature, there are many colors of noise. However in astronomy, we talk about either white noise (where the periodogram shows no significant signal and the powers are well modeled by a power law index of 0) or red noise, where the power follows a power law index  $> 0$ . To calculate the real significance of a signal, it is important to quantify the contribution of the red noise. To do this, one can normalize the power spectra by the true underlying spectra (i.e., the expectation value of the power spectra; see, e.g., Vaughan, 2005). For the intervals considered in this paper, the overall power law index of the periodogram is  $\sim 0$  through the whole frequency range, and therefore, red noise is not affecting the significance of QPO detections (see; Jackman et al., 2018 for more details). The location of the origin of the pulsations found in this study is mapped out using the model created by Vogt et al. (2011), and the results are shown in section 3.4.

To further improve the significance of the signals found, we tested the sensitivity of the light curve to frequency in this study using a Jackknife test (Quenouille, 1949, 1956). This is carried out by removing a number of photons from the HS1 and HS2 light curves and running the Rayleigh test again on each new light curve (Efron & Stein, 1981). All the power spectra are then plotted together and the distance between the minimum and maximum period found provides an estimate of how sensitive the light curve is to frequency. As Chandra observes very few photons from Jupiter, the Jackknife test used in this study removed three photons each time, ensuring no degeneracy from the selection process. The test for HS1 and HS2 found the time between the lowest and highest best period to be  $\Delta P = 0.9809$  and 1.3765 min, respectively. For both HS1 and HS2,  $> 10^7$  power spectra are generated using the Jackknife test. This small shift in period over these many trials shows that the derived QPO frequencies are quite robust. There was an  $\sim 5$ -hr overlap with XMM-Newton from 19 June  $\sim 00:20$ – $05:15$  where QPOs can be compared. During this interval, XMM-Newton found the same QPO at  $\sim 28$  min increasing our confidence in the HS2 signal detected by Chandra. XMM-Newton continued observing for  $\sim 16$  hr after Chandra, and examination of the light curve from that time interval indicates that the same QPO is still present for another full rotation (details discussed further in Wibisono et al. (submitted, 2019)). Performing the Rayleigh test discussed in this study on the full XMM-Newton light curve, we find a 99.92% significant  $\sim 28$ -min QPO.

Figure 7 shows the light curve and results from the same Rayleigh test used to analyze the southern region. As shown in Figure 7b, the best quasiperiod found from the full light curve of the southern region is  $\sim 92$  min and had a significance of 24.30% ( $p$  value 0.7570 or 7,570 out of 10,000 results from test greater than peak power). A downselect of location is not used in the analysis as the emission is too diffuse and there are insufficient counts in the south. The large  $p$  values found in the southern region demonstrate that the best periods found from the Rayleigh test are not significant. This is further illustrated in Figure 7c, which compares the highest power found with the red cumulative distribution curve. The best period and its associated highest power from the Chandra South pole data lies near the peak of the expected random distribution of photons. This therefore suggests that this is not a significant signal, and unlike the northern extended hot spot, there are no significant quasiperiods found during the observation.

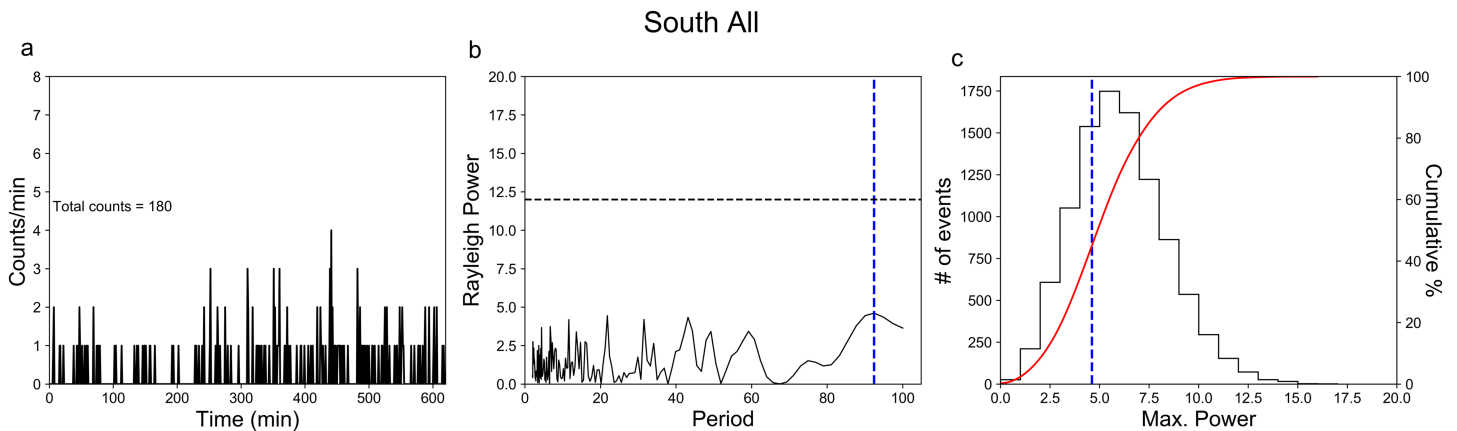


**Figure 7.** (a–c) Timing analysis for the southern auroral region, in the same format as Figure 6.

### 3.3. Accompanying In Situ Juno Data

Around the time of our Chandra observations, Juno was executing a series of orbits which took the apoJove to  $\sim 112 R_J$  on the dawn flank of Jupiter's magnetosphere, near the nominal magnetopause position. This allows possible auroral drivers like KHI and magnetopause reconnection to be explored. Figure 8 shows the JADE data over a 5-day period bracketing the Chandra interval. The top panel is the time-of-flight mass spectrometer data of ion populations during this interval, and the middle panel shows the corresponding electron distributions. The color bars in both plots represent the count rates (proportional to energy flux) of the electrons and ions detected. The bottom panel shows the radial distance of Juno from Jupiter during the observation. Arrows at the top of the plot show the region (e.g., magnetosphere and magnetosheath) which Juno was sampling at a given time, and the Chandra observation interval is also highlighted by dashed vertical lines.

From the JADE data, a magnetopause crossing is defined as a steep change in density or intensity of the ion plasma population when Juno crosses from a region of colder, dense plasma (magnetosheath) to one of hotter, rarer plasma (magnetosphere) and vice versa. Figure 8 shows that, while Juno was inbound from apoJove, there are several magnetopause crossings preceding the Chandra observations. Juno was found to cross the magnetopause, from the magnetosphere, at  $\sim 14:30$  on day 167 (16 June) and found again to cross back into the magnetosphere at  $\sim 14:00$  on day 168 (17 June). Another crossing out into the magnetosheath was detected by JADE at  $\sim 09:00$  on day 169 (18 June), and thereafter, Juno was found to be in the magnetosheath until shortly before the end of the Chandra observation. Within the Chandra observation window, a short crossing into the magnetosphere was detected between  $\sim 00:00$  and  $\sim 01:00$  on day 170. Juno crossed back into the magnetosphere  $\sim 03:30$  with no further crossings detected during the 5-day window. JEDI data were also examined during this observation window and found to confirm the approximate time line of the magnetopause crossings illustrated by JADE.

To infer the state of compression of the Jovian magnetosphere during the Chandra interval, the Joy et al. (2002) model is used to find the most probable subsolar standoff position of the magnetopause boundary. The Joy et al. (2002) magnetopause and bow shock model is a very powerful tool that allows us to infer the dynamic pressure of the upstream solar wind and corresponding subsolar standoff distance from the location of any crossing the magnetopause boundary. The model was created by combining multiple spacecraft observations (Pioneer 10 and 11, Voyager 1 and 2, and Ulysses and Galileo) with magnetopause encounters with a magnetohydrodynamics simulation. The spacecraft data were used to determine the probability that regions surrounding Jupiter fall within or outside the boundaries calculated from the magnetohydrodynamic simulations, parameterized by the solar wind dynamic pressure. Using the closest magnetopause crossing from the JADE data ( $\sim 111 R_J$ , 4.4 LT), the Joy et al. (2002) model inferred that the dynamic pressure of the solar wind,  $P_{\text{dyn}}$ , during this time (day 170,  $\sim 03:00$ ) was 0.319 nPa and the subsolar standoff distance,  $R_{\text{MP}}$ , was  $62.52 R_J$ . Comparing these inferred solar wind parameters to distributions of the solar wind upstream from Jupiter from Jackman and Arridge (2011) and Ebert et al. (2014) shows that the magnetosphere during this time was in a state of compression, well above the 90th percentile of previously observed solar wind dynamic pressures.

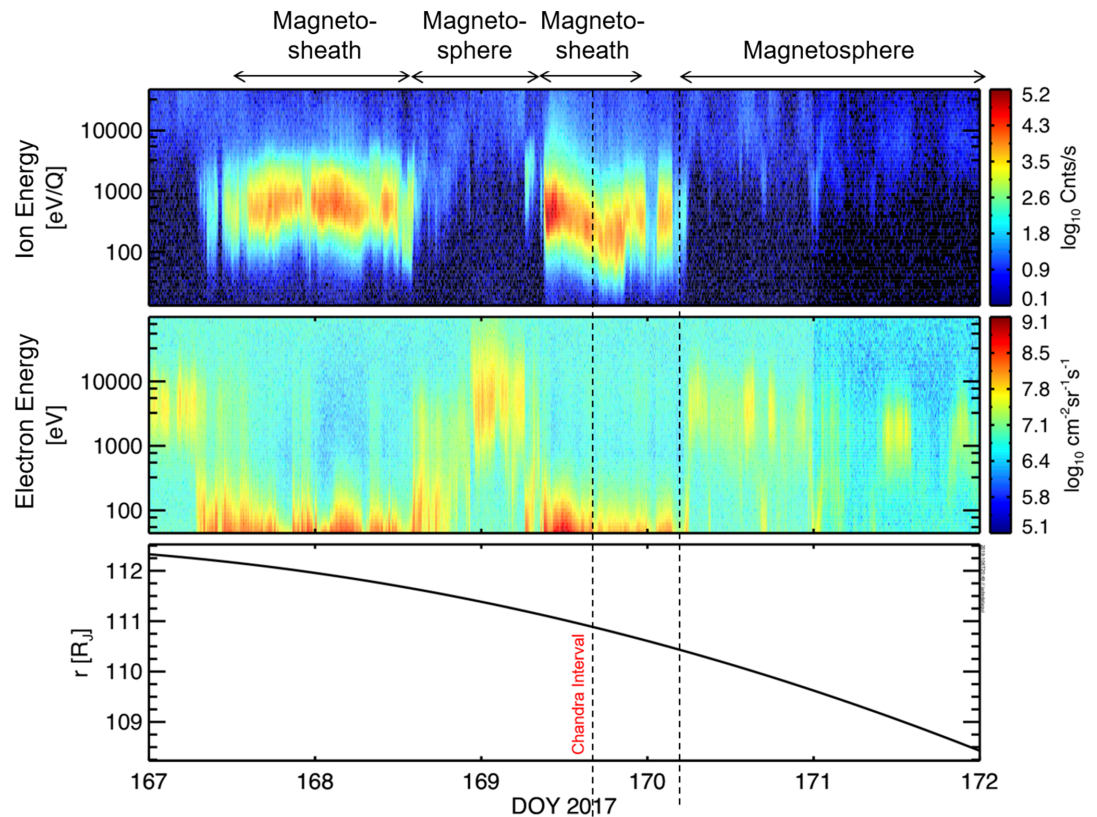


**Figure 8.** The ion time of flight (TOF) and electron data taken by Juno JADE for 5 days while inbound from apojoive. The top panel shows ion data from the different plasma populations in the magnetosheath and magnetosphere. The middle panel shows the corresponding electron distributions within the system, and the bottom panel indicates the radial distance of the spacecraft from Jupiter during the observation. The Chandra interval is shown by the vertical dashed lines. The color bars represent the count rates (proportional to energy flux) of the electrons and ions detected during this time. The key regions Juno entered are denoted by the arrows above the plot.

### 3.4. Vogt Mapping Results

To map the origin of the hot spot photons and in turn the QPOs, the ionospheric position (S3 longitude and latitude) and subsolar longitude (SSL) of the time-tagged hot spot photons are used in a flux equivalence mapping model created by Vogt et al. (2011, 2015). The Vogt et al. (2011, 2015) flux equivalence mapping model relates a position in the ionosphere to a source region in the equator (radial distance and LT). This model is based on the assumption that the flux through a given region in the jovigraphic equator, which is calculated using a 2-D fit to Galileo data, should match the flux through the ionosphere in the region to which it maps. The mapping depends on SSL. We use the Vogt et al. model with the JRM09 internal field model option.

The Vogt model is built from data, and its region of validity extends from  $\sim 15 R_J$  (Ganymede footprint) to  $\sim 150 R_J$  (beyond which there were insufficient data to constrain the model). Figure 9a shows the polar plot of the mapped (black circles) and unmapped equatorial (black triangles) and auroral (orange triangles) photons over the full Chandra interval. Figure 9b illustrates the resulting magnetospheric mappings using the flux equivalence model for all auroral photons for which such mapping is possible during the full Chandra observation. Rows (c, d) and (e, f) are in a similar format for the intervals corresponding to the viewing of HS1 and HS2. The Ganymede footprint is represented as a black oval in Figures 9a, 9c, and 9e. The colored contours plotted in Figure 9a show how the magnetic field mapping of the  $90 R_J$  and  $150 R_J$  radial distances changes during the full Chandra observation at  $120^\circ$  SSL intervals from  $130^\circ$  to  $10^\circ$  SSL during approximately one Jovian rotation. At the beginning of the observation ( $130^\circ$  SSL), the dayside magnetosphere is on the right-hand side of the polar plot and moves clockwise throughout the Chandra interval. Figures 9c and 9e show the position of the magnetic field mapping midway through the hot spot intervals ( $170^\circ$  and  $110^\circ$  SSL, respectively). Photons that have ionospheric positions equatorward of the Ganymede footprint are not

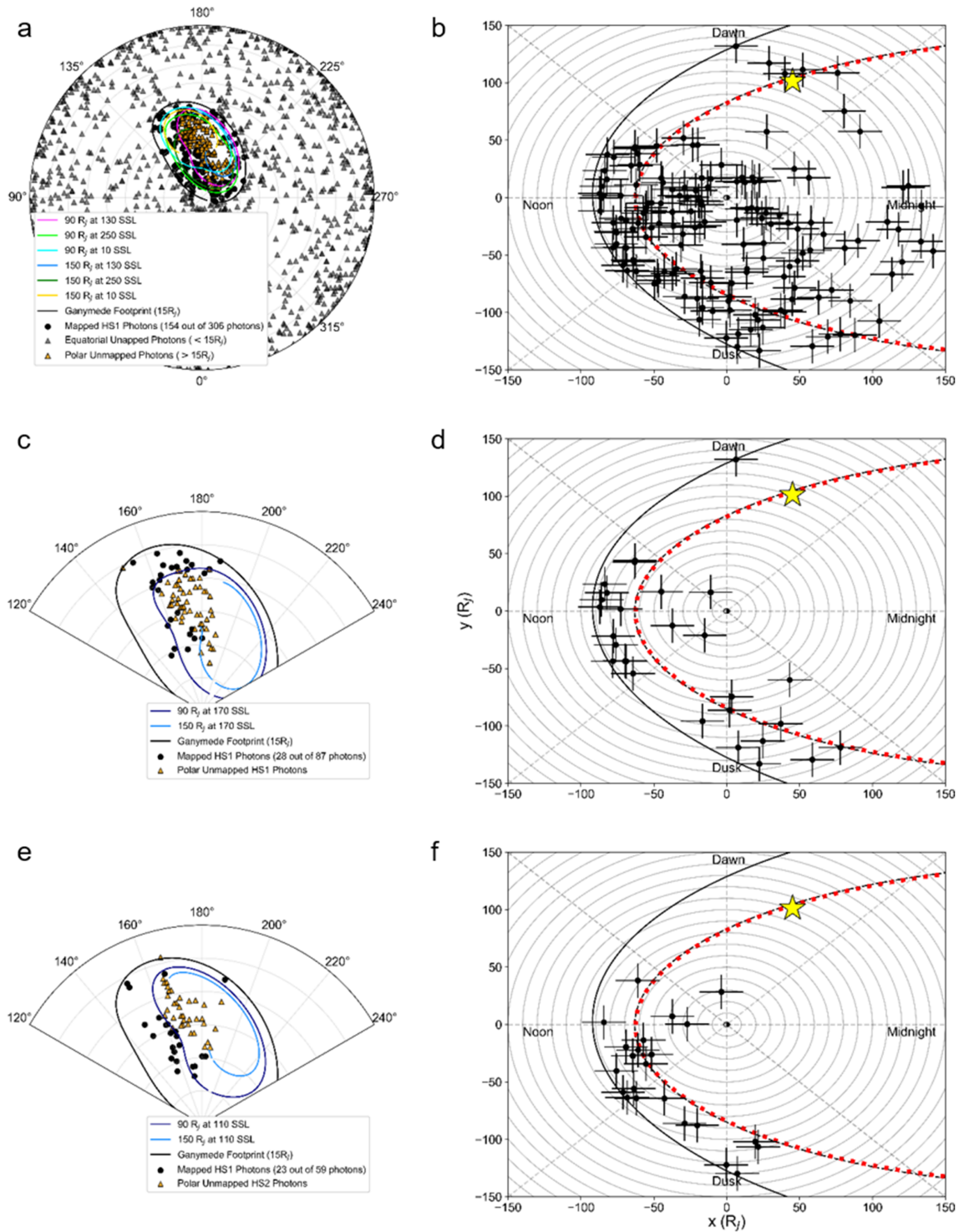


**Figure 9.** Polar plots of Jupiter's north pole for (a) all auroral photons during the full observation and the hot spot photons associated with (c) HS1 and (e) HS2 defined in section 3.1. The origins of the photons during each interval are calculated using the (Vogt et al., 2011, 2015) model shown in panels (b), (d), and (f). Error bars of 15  $R_J$  are used to represent the likely error in the Vogt flux equivalence mapping model, under compressed magnetospheric conditions. The 15  $R_J$  (black oval), 90  $R_J$ , and 150  $R_J$  of the flux equivalence model using the JRM09 internal field (Connerney et al., 2018) are plotted in (a), (c), and (e) at different subsolar longitudes (SSLs). Unmapped photons equatorward (<15  $R_J$ ) and poleward (>15  $R_J$ ) are denoted by black and orange triangles, respectively. The different colors in (a) show the 90 and 150  $R_J$  contours observed at different SSLs throughout the interval. Panels (c) and (e) show the 90  $R_J$  (navy line) and 150  $R_J$  (light blue line) contours midway through the interval. The location of Juno is denoted by the yellow star. The concentric ellipses in (b), (d), and (f) represent the distance from Jupiter in 10  $R_J$  increments. The subsolar standoff distance inferred from the Joy et al. (2002) magnetospheric model from the Juno crossings is plotted in red (at 62.52  $R_J$ ), as well as the compressed (black dashed line) and expanded boundary limits.

mapped by the flux equivalence. The  $90 R_J$  and  $150 R_J$  contours are indicated in navy and light blue, respectively. Contours mapping to  $90 R_J$  in the equator and beyond are not drawn for positions where they would map to points beyond the Joy et al. (2002) expanded magnetopause. The Vogt et al. (2011) model is not valid for mapping beyond  $150 R_J$  because this is the limit of the magnetic field data coverage in the Jovian magnetotail. The photons shown in gray in Figure 9, which we refer to as “unmapped,” are so called because their ionospheric positions are linked to radial distances in the magnetosphere that lie beyond the expanded Joy et al. magnetopause or the  $150 R_J$  limit of the model. It is therefore likely that these ionospheric positions are on open field lines. Photons that have ionospheric positions equatorward of the Ganymede footprint are not mapped by the flux equivalence model as they map to radial distances inside  $15 R_J$ .

Figures 9b, 9d, and 9f show the positions of the mapped photons determined from the flux equivalence model within the Jovian magnetosphere. The dynamic pressure inferred from the Juno magnetopause crossings is used to plot the position of the magnetopause during this time with an inferred subsolar standoff distance of  $62.52 R_J$  (shown by the red dotted line). Our inferred magnetopause boundary coincides with the subsolar standoff distance limit in the Joy model for a compressed magnetosphere (0.306 nPa with subsolar standoff distance  $\sim 60 R_J$ ; black dashed line). The Joy model limit of an expanded magnetosphere is represented by the solid black line (0.039 nPa with nose standoff distance  $\sim 90 R_J$ ). The approximate position of Juno during the Chandra interval is denoted by a yellow star.

Figure 9b shows the spread of the mapping throughout the magnetosphere (154 out of 306 auroral photons are mapped). The Vogt flux calculation uses a fit to Galileo data that were collected under all solar wind conditions, and therefore, the mapping represents an “average” magnetospheric state. In this study, we consider any ionospheric points that map to the magnetospheric positions between the compressed and expanded Joy et al. magnetopause values (the black dashed and solid lines, respectively, in Figure 9) in our analysis. We interpret these points to map on closed field lines for an expanded magnetosphere/low solar wind dynamic pressure and on open field lines for a compressed magnetosphere/high solar wind dynamic pressure. As the model is based on the solar wind conditions throughout the Galileo mission, the magnetosphere of the Jupiter would have been mainly in an expanded state or returning to equilibrium position during the majority of the mission. Therefore, the mapping in Figure 9 is probably not quite right for the highly compressed conditions of the Chandra observation interval. Since the model maps only to points that lie within the magnetosphere (i.e., on closed field lines), we assume that the points in Figure 9 that lie outside the compressed magnetopause would probably actually map to a region near but inside the magnetopause if the compressed conditions were accounted for. From the mapping model, however, we cannot determine accurately whether the QPOs found lie on open or closed field lines.

During intervals of high solar wind dynamic pressure and a highly compressed magnetosphere, as was the case during these observations, we may expect the change in the magnetospheric field geometry to lead to a change in auroral mapping (e.g., Cowley & Bunce, 2003a, 2003b; Southwood & Kivelson, 2001). Following an increase in the solar wind dynamic pressure, the observed changes in Jupiter’s magnetospheric magnetic field are sufficient to shift the auroral mapping of a given point in the magnetosphere poleward by up to a few degrees (Vogt et al., 2019). Therefore, we estimate a  $15 R_J$  uncertainty in the mapping of our X-ray photons (see Figure 9) to account for this effect.

Figures 9d and 9f show that the majority of mapped photons from the HS1 (28 out of 87 auroral photons are mapped) and HS2 (23 out of 59 auroral photons are mapped) intervals are found to originate in the noon-dusk magnetosphere, close to the magnetopause boundary within  $90 R_J$ . This suggests that the origin of the processes that create the hot spot (and in turn the QPOs) may occur on the noon-dusk boundary also. The corresponding polar plots, panels (c) and (e), show that the majority of the unmapped photons are found to lie beyond the dayside magnetopause boundary. More specifically, this is the case when the SSL is between  $100^\circ$  and  $200^\circ$ , which occurs for the full HS1 interval and the latter part of the HS2 interval. This may suggest that the origin of some the X-ray emissions, hence many of the unmapped photons, is in the magnetopause where flux is opened for a short period of time (McComas & Bagenal, 2007). The possibility of an open field line origin for the X-ray emissions is discussed further in section 4. One caveat that supports this hypothesis is taken into account in our analysis. The flux equivalence model assumes average solar wind conditions, where the Jovian magnetosphere will be found to be observed mainly rarefied or relaxing from a compressed state. Therefore, many unmapped points close to the  $90 R_J$  contour on the dayside magnetosphere may map

to inside, or very close to, the magnetopause. Alternatively, many mapped photons found in this region may actually be on open field lines. At lower SSLs found at the beginning of the HS2 interval, 70–100° SSL, some of the unmapped photons are also found to lie on field lines on the nightside beyond 150  $R_J$ . These field lines may be considered opened or closed, but the lack of data in this region makes verification of this difficult. The unmapped photons that are found firmly in the middle of the open field area are considered to definitely be on open field lines. The photons producing the pulsations within the magnetosphere in both intervals are also found to lie in approximately the same locations. This further suggests that the photons responsible for the pulsations in HS1 and HS2 may be a result of a process happening near the dayside magnetopause that varies on timescales less than a Jupiter rotation. Panel (d) shows that the pulsations during the HS1 interval are slightly more spread throughout the magnetosphere than those observed during HS2 (panel f)) with the pulses mapping to ~11–22 LT compared to the pulses originating mainly in the noon-dusk sector. The pulsations appear to map to spatially localized regions in the magnetosphere as shown by the clustering of mapped photons within the noon-dusk sector present in Figures 9d and 9f.

#### 4. Discussion

The results of our study analyzing the ~10-hr Chandra Jupiter observation from 18:56, 18 June 2017, using a new Python pipeline, reveal an interesting extended morphology of the northern hot spot that has not been studied in great detail before.

The polar plots that we present in this study show a clear asymmetry in brightness between the north and south poles. Dunn et al. (2017) found that the morphology of the southern X-ray aurora and unfavorable tilt angle of Jupiter made it very difficult to observe, which is why very few observations of the South have been presented in previous studies. In this study, however, the full southern region is mapped, allowing for direct comparison with the north. The JRM09 magnetic field model (Connerney et al., 2018) is derived from Juno magnetometer data (Connerney et al., 2017) and revealed that the field in the north polar region is nondipolar and more than twice as strong as the more dipole-like field in the south (Moore et al., 2018). This contrast in magnetic field strength and topology may be a contributing factor to the clear difference in brightness between the poles, as well as the diffuse nature of the X-ray emission observed from the south pole. The different magnetic field magnitude may inject ions into the Jovian ionosphere through a variety of mechanisms. It may be that the stronger magnetic field in the north leads to a stronger mirror force and therefore produces a larger potential drop, capable of accelerating ions to larger energies. Alternatively, it may be that the steeper magnetic field gradients in the north allow drifting particles to enter the loss cone. Given the location of the extended X-ray hot spot relative to the surface magnetic field configuration, we suggest that the former is more likely. Along with the contrast in brightness, the independent nature of the pulsations (observed here and in Dunn et al., 2017) suggests that the emission from the north and south may be from different processes or the same process triggered independently (from a possible time lag) either side of the magnetopause boundary.

In this study, we find two significant QPOs in the light curve from the north pole when the elongated hot spot is in view (North HS1 and HS2) using a Rayleigh test. Using the same Rayleigh test for the south, we found no significant QPOs during this time. However, the XMM-Newton telescope continued to observe Jupiter for a further ~18 hr after the end of the Chandra campaign. This data set is explored in detail in Wibisono et al. (submitted, 2019). They note that Jupiter continued to pulse with a regular QPO for several Jupiter rotations after this observation.

Dunn et al. (2017) suggest that KHIs observed at Jupiter's magnetopause boundary (Delamere & Bagenal, 2010; Desroche et al., 2012) may be one possible driver to explain the Jovian quasiperiodic X-ray emissions and the asymmetric brightening at the poles. The KHIs on a planet's magnetopause boundary allow large quantities of energy, momentum, and plasma to be transferred between separate plasma media and may cause reconnection in the twisted field lines (Hasegawa et al., 2004). KHIs on Earth's magnetopause have been found to produce fluctuations in the magnetopause and compressional ultralow frequency oscillations and field line resonances (on closed field lines), driving standing Alfvén waves in the ionosphere (Mann et al., 2002; Rae et al., 2005). Previous observations and simulations have found that KHIs often originate on the dawn and dusk flanks of the magnetosphere, where the velocity shear is largest. This has been found to be the case at both Earth and Saturn (Hasegawa et al., 2004; Ma et al., 2015; Wilson et al., 2012) as well

as predominantly on the duskside at Jupiter (Zhang et al., 2018). In this study, as shown in Figure 9, many of the photons which yield the QPOs are mapped to regions near, or within, the magnetopause boundary on the dusk flank of the magnetosphere. However, with the mapping model not optimized for very compressed magnetospheric conditions, distinguishing between the origin lying on open or closed field lines is difficult. Dunn et al. (2017) found that the northern and southern X-ray hot spots exhibited different temporal behavior. Using the Vogt et al. (2011, 2015) flux equivalence mapping model, Dunn et al. (2017) also find that the majority of the northern X-ray photons map onto the dayside magnetopause boundary on the noon-dusk side. The southern X-ray emissions were found to map to the magnetopause boundary on the dawn-noon sector, indicating that the processes producing the QPOs at the poles may be independent of one another. This may be explained by rotationally driven magnetic reconnection on the dayside magnetodisk. Guo et al. (2018) report finding such a phenomenon in Saturn's dayside magnetodisk from Cassini charged particle and magnetometer data. This internally driven process could, in theory, accelerate the high-energy ions in the Jovian system to the energies required for the production of X-rays and explain the flaring activity we observe in the aurora (in both X-ray and UV; e.g., Bonfond et al., 2016). Rotationally driven dayside reconnection and reconnection driven by KHIs on the dawn/dusk flanks occur in different regions of the magnetosphere and may be the answer to the observed nonconjugacy of the north and south emissions in this study.

Previous studies looking at the hot spot region (Dunn et al., 2016, 2017; Gladstone et al., 2002; Kimura et al., 2016) speculate that oscillations may arise from global ULF waves in the magnetic field. The periodic oscillations from ULF waves have been observed throughout the Jovian magnetosphere. Manners et al. (2018) propose that all  $\sim 10$ - to 60-min QPOs within the Jovian magnetosphere may arise from standing Alfvén waves. This complements the work of Khurana and Kivelson (1989) and Wilson and Dougherty (2000) who found 10- to 20-min ULF wave pulsations in the middle magnetosphere. The QPOs we observe in this study and previous statistical studies (Jackman et al., 2018) lie within the 10- to 60-min range. This would apply to regions of closed field lines where Alfvénic resonances are present. For open field line regions within the magnetosheath, dawn/dusk flank reconnection may produce the pulsations we observe in the X-rays. The reconnection process in this region of the magnetosphere may be triggered by KHIs on the flank, producing possible field line resonances generating the QPOs we observe (Dunn et al., 2016, 2017; Kimura et al., 2016). Magnetic reconnection along the dawn flank of the magnetosphere has been reported before by Ebert, Allegrini, Bagenal, Bolton, Connerney, Clark, DiBraccio, et al. (2017) where it plays a more significant role within a compressed magnetosphere (high solar wind dynamic pressure). However, as Juno was not on the dusk flank of the magnetosphere, signatures of magnetic reconnection during this time cannot be found. The cusp reconnection model by Bunce et al. (2004) provides a strong argument for the possible origin of strong X-ray emission with 40- to 50-min QPOs. The significant periods found in this study lie close to this temporal range (in particular the  $\sim 37$ -min quasiperiod from the first viewing of the northern hot spot, HS1). The X-rays observed in this study however only have a maximum brightness of a few Rayleighs (R) as opposed to  $\sim kR$  magnitudes predicted by the cusp reconnection model. Therefore, cusp reconnection may provide an answer to the pulsations we observe, estimating an upper limit for the X-ray auroral power and brightness. We observe the expected X-ray auroral power (approximately few GW) predicted by Bunce et al. (2004), but our observed auroral brightness is inconsistent with their model. This inconsistency may be a result of us underestimating the auroral brightness due to the poor throughput of the Chandra HRC-I instrument and/or the atmosphere possibly being highly opaque during the Chandra interval (Ozak et al., 2010).

The two different significant quasiperiods in the north suggest that the process(es) that cause the flaring activity in the X-rays can change over a timescale less than one Jovian rotation. Only a small number of X-ray observations are conducive to searching for variability in quasiperiodicity on the timescales of a few planetary rotations or less. From the Jackman et al. (2018) heritage study, one observation was found ( $\sim 20$  hr observation from 00:21, 25 February 2003) where the cadence of the telescope observation allowed the northern and southern hot spots to be viewed separately on consecutive rotations. From the Rayleigh test, they found that the only significant QPO was when the northern hot spot was first in view at  $\sim 33$  min. The second time the northern hot spot was in view, no significant quasiperiodic signal was found. They found that only one other example ( $\sim 11$ -hr observation from 08:18, 8 April 2014) exhibited different significant quasiperiods in the south over a timescale less than one Jovian rotation. Therefore, our study is the first to analyze multiple significant QPOs in the northern hot spot, and the conditions for the driver to produce



such emission may have been rarely observed. Jackman et al. (2018) also noted that not many of the QPOs

found in previous studies were actually statistically significant using the Rayleigh test.

The quickening of the pulsations during this observation may be a result of the changing conditions of the magnetosphere. If we consider ULF waves to be the source, the changing periodicity of the QPOs would be a result of the changing thickness of the plasma sheet (Manners et al., 2018). During a compression event (similar to that found in the Juno data preceding the Chandra interval), the plasma sheet is expected to thicken (Southwood & Kivelson, 2001) which in turn will result in a longer QPO (Manners et al., 2018). As the magnetosphere enters the recovery phases after the compression, the thickness of the plasma sheet decreases as does the period of the QPO. However, with the data we have, it is unclear how quickly the plasma will be ejected from the magnetotail to confirm this ULF wave process. The inverse is true if we consider the Bunce et al. (2004) reconnection model.

During a compression event, the field line that the MeV ions travel along into the ionosphere will become shorter, therefore reducing the Alfvén time and generating a quicker QPO. If we assume that the reconnection site is in the same LT along the magnetopause and that the magnetosphere is further compressed between both HS1 and HS2, this may also be an answer to the changing periodicity in this study. However, from the Juno JADE and JEDI data, we find the magnetosphere expanding between HS1 and HS2, ruling this mechanism out. From terrestrial observations, the orientation of the interplanetary magnetic field and latitude of the reconnection site can also change the topology of the magnetic field and can therefore change the periodicities produced by cusp reconnection processes (Gosling et al., 1990; Fuselier et al., 2012). This may be the case in this study; however, the limitations with our data prevent us from being able to give a clear answer of the location of possible reconnection sites close to the mapped photons in the dusk flank.

In this study we believe that the QPOs observed are more likely caused by ULF waves on the dusk flank of the magnetosphere, produced by possible KHIs. However, it is unclear if this is true for all QPOs observed from the X-ray emission as this conclusion is based on one observation. Future work into determining the source of the pulsations may include a comparison between transit times during compression and expansion for both ULF waves and reconnection processes described by Bunce et al. (2004). This can then be compared to possible statistical studies looking into times of magnetopause compressions to find the more dominant process in tandem with future Juno observations. Juno is expected to be in the dusk sector from 2021, allowing these processes to be explored in detail on the dusk flank of the magnetosphere close to the possible mapped location of the driver we find in this study.

The significant number of unmapped photons in both intervals (~68% and ~61% for HS1 and HS2 of hot spot photons, respectively) may suggest the driver for the X-ray emissions; thus, the QPOs are located on open field lines in a region near but inside the magnetopause during a compression event (similar to Dunn et al., 2016). This however does not provide an answer for the variability of the driver found in this study. Given the significant number of unmapped hot spot photons combined with the successfully mapped QPOs to the noon-dusk sector, and with Juno situated on the dawn flank of the magnetosphere during this time (where only a handful of photons have been mapped to with an error on radial distance due to compressed conditions, as shown in Figure 9), this precludes us from being able to fully determine the auroral driver. If Juno's trajectory was closer to the noon-dusk sector, where the vast majority of photons were mapped to or crossed field lines connected to the polar position of the X-ray emissions, further analysis of the in situ energetic particle data would have been included in our study. The very energetic particles (up to MeV energies) found in the polar auroral region detected by Juno are believed to lie on possible open field lines (Ebert, Allegrini, Bagenal, Bolton, Connerney, Clark, Gladstone, et al., 2017), suggesting that some process producing (or accelerating) these particles must exist. However, some studies suggest that the opened flux may close rapidly under such magnetospheric conditions (McComas & Bagenal, 2007). As this is not the main focus of the paper, future work (in concert with analysis of in situ Juno data) may seek to delve into more detail on the possible drivers of the X-ray emission (both on open and closed field lines) and specifically in links to quasiperiodic processes.

The possibility of the source lying along the open-closed field lines agrees with results from Dunn et al. (2016). They observed a significant ~26-min QPO during the arrival of an interplanetary coronal mass ejection at Jupiter (i.e., a compression event). The hot spot was found to be extended, and an expansion occurred on field lines that mapped to the region where the magnetopause subsolar standoff distance was found to move from 92 to 63  $R_J$  (from the Joy et al., 2002 model). Using the equivalence mapping model, Dunn

et al. (2016) found that the majority of X-ray producing ions originated beyond  $60 R_J$  where most of the carbon/sulfur emission was found to originate on open field lines between  $50$  and  $90 R_J$  (for the case of a compressed magnetosphere). The 26-min QPO was observed to originate on the edge of the hot spot (between  $150^\circ$  and  $160^\circ$  S3 longitude) and was strong in carbon/sulfur emission. This was speculated to be the source of the brightening in this region. Comparing the Dunn et al. (2016) results to our study, both observe a significant  $\sim 26$ -min QPO during an inferred compression event and find that the majority of X-ray producing ions originate  $>60 R_J$ . The observed brightening at the edge of the expanded hot spot region by Dunn et al. (2016) may also suggest that there are multiple independent X-ray sources producing this variable emission (as suggested by Figure 3 in this study) during a compression event.

The Juno data set affords us the unique opportunity to have a window on the magnetosphere (or upstream environment) to provide important context for the X-ray observations which has been missing in previous years. From in situ Juno data, we can infer the condition of the Jovian magnetosphere and have a better understanding of what possible drivers are producing the hot spot emission. When Juno is nearer the polar regions, JEDI will allow us to detect and analyze the MeV ions that we expect to underpin the X-ray aurora mechanism. Houston et al. (2019) start to investigate the MeV polar ions in the context of X-ray emissions to help use the in situ data to provide a vital contribution on trying to answer the origin of the soft Jovian X-rays and their corresponding (quasi-) pulsating driver.

An emergency reset of Hubble Space Telescope meant that a UV observation which was scheduled to overlap with this X-ray campaign did not happen. Thus, we unfortunately lost the ability to compare the X-ray QPOs with the UV waveband for this case. The emergency reset itself was possibly triggered by an intense solar event on Jupiter (perhaps associated the inferred solar wind compression during this interval). Future multiwavelength campaigns during the Juno era should shed light on the relationship between X-ray, UV, and other wavebands and on the distinct physical processes which cause these diverse emissions.

It is clear that further work is required to fully understand the driver of Jupiter's X-rays, and future studies will need to make more comparisons with UV and radio data. The processing pipeline and numerical hot spot definition employed in our study combined with Juno in situ data can be used to examine any correlations between the varying morphology and intensity of the hot spot with the multitude of different factors that may affect the Jovian X-ray emission. These techniques will also allow a more consistent comparison to be made between all the Chandra data in great detail. This study provides new information on where the ions originate, although more data are needed to determine where on the field lines the acceleration takes place. Comparisons with factors such as solar activity and magnetospheric state will allow us to determine what conditions produce the different X-ray emission morphologies we have observed and allow us to fully understand the true origin of Jupiter's X-rays.

## 5. Summary

From the expanding catalog of Chandra observations of Jupiter X-rays during a variety of solar wind and magnetospheric conditions, this is the first study analyzing an extended northern hot spot emission in great detail during a solar wind compression. Previous works have found a hot spot of emission in both the north and south poles, but the intensity and elongation of the northern hot spot during this interval are unique. With accompanying in situ Juno data, we can provide the Chandra observations with magnetospheric context allowing us to attempt to identify what conditions are needed to produce the various morphologies of the X-ray aurora and find their origin. Our results reveal statistically significant QPOs from the northern hot spot, with period varying from  $\sim 26$  to  $37$  min during two separate viewing windows separated by less than a planetary rotation. These pulsating X-ray photons map to a region close to the dayside magnetopause which points to processes in that region as a likely driver to the X-ray behavior.

We hope that the work presented here will provide another avenue analyzing the morphology and intensity of the hot spot emission using a numerical definition with more robust timing analysis in the Juno era. The combination of these techniques with multiwavelength remote sensing and in situ data will allow us to finally understand the physics of the drivers producing these dynamic emissions. We look forward to exploring further the conditions that produce the varying morphologies of the hot spot and the range of significant QPOs observed throughout Chandra's ongoing Jupiter campaign.

**Acknowledgments**

D. M. W. is supported by the Science and Technology Facilities Council (STFC) studentship ST/S505705/1. C. M. J.'s work at Southampton was supported by the STFC Ernest Rutherford Fellowship ST/L004399/1. C. M. J.'s work at DIAS was supported by the Science Foundation Ireland Grant 18/FRL/6199. M. F. V. was supported by the Juno Participating Scientist Program (Grant 80NSSC19K1263) and by NASA Grant 80NSSC17K0777. W. R. D is supported by STFC Project ST/S000240/1 and by the European Space Agency (ESA) Contract 4000120752/17/NL/MH. D. A acknowledges support from the Royal Society (Grant URF R 180001). We use the pipeline code from <https://github.com/waledeigt/zeno-py> Web site. D. M. W acknowledges support from JADE and JEDI teams for providing the plots needed to provide vital context to the Chandra data and their help analyzing the electron and ion data. This research has made use of data obtained from the *Chandra Data Archive* and *Chandra Source Catalogue* (<https://cda.harvard.edu/chaser/>) as well as software provided by the Chandra X-ray CIAO. The data used to create the Chandra plots shown in this paper can be found online (<https://doi.org/10.5258/SOTON/D1222>). The Juno JADE data were obtained from the NASA *Planetary Data System* (<https://pds-ppi.igpp.ucla.edu/mission/JUNO/JNO/JAD>).

**References**

Bhardwaj, A., Branduardi-Raymont, G., Elsner, R. F., Gladstone, G. R., Ramsay, G., Rodriguez, P., et al. (2005). Solar control on Jupiter's equatorial X-ray emissions: 26-29 November 2003 XMM-Newton observation. *Geophysical Research Letters*, *32*, L03S08. <https://doi.org/10.1029/2004GL021497>

Bhardwaj, A., & Gladstone, G. R. (2000). Auroral emissions of the giant planets. *Reviews of Geophysics*, *38*(3), 295–353. <https://doi.org/10.1029/1998RG000046>

Bolton, S. J., Lunine, J., Stevenson, D., Connerney, J. E. P., Levin, S., Owen, T. C., et al. (2017). The Juno mission. *Space Science Reviews*, *213*(1–4), 5–37. <https://doi.org/10.1007/s11214-017-0429-6>

Bonfond, B., Grodent, D., Badman, S. V., Gérard, J. C., & Radioti, A. (2016). Dynamics of the flares in the active polar region of Jupiter. *Geophysical Research Letters*, *43*, 11,963–11,970. <https://doi.org/10.1002/2016GL071757>

Branduardi-Raymont, G., Bhardwaj, A., Elsner, R. F., Gladstone, G. R., Ramsay, G., Rodriguez, P., et al. (2007a). Latest results on Jovian disk X-rays from XMM-Newton. *Planetary and Space Science*, *55*(9), 1126–1134. <https://doi.org/10.1016/j.pss.2006.11.017>

Branduardi-Raymont, G., Bhardwaj, A., Elsner, R. F., Gladstone, G. R., Ramsay, G., Rodriguez, P., et al. (2007b). A study of Jupiter's aurorae with XMM-Newton. *Astronomy and Astrophysics*, *463*(2), 761–774. <https://doi.org/10.1051/0004-6361/20066406>

Branduardi-Raymont, G., Elsner, R. F., Galand, M., Grodent, D., Cravens, T. E., Ford, P., et al. (2008). Spectral morphology of the X-ray emission from Jupiter's aurorae. *Journal of Geophysical Research*, *113*, 1–11. <https://doi.org/10.1029/2007JA012600>

Branduardi-Raymont, G., Elsner, R. F., Gladstone, G. R., Ramsay, G., Rodriguez, P., Soria, R., & Waite, J. H. (2004). First observation of Jupiter by XMM-Newton. *Astronomy*, *337*(1149), 331–337. <https://doi.org/10.1051/0004-6361>

Brazier, K. T. S. (1994). Confidence intervals from the Rayleigh test. *Monthly Notices of the Royal Astronomical Society*, *268*(3), 709–712. <https://doi.org/10.1093/mnras/268.3.709>

Bunce, E. J., Cowley, S. W. H., & Yeoman, T. K. (2004). Jovian cusp processes: Implications for the polar aurora. *Journal of Geophysical Research*, *109*, 1–26. <https://doi.org/10.1029/2003JA010280>

Connerney, J. E. P., Benn, M., Bjarno, J. B., Denver, T., Espley, J., Jorgensen, J. L., et al. (2017). The Juno magnetic field investigation. *Space Science Reviews*, *213*(1–4), 39–138. <https://doi.org/10.1007/s11214-017-0334-z>

Connerney, J. E. P., Kotsiaros, S., Oliverson, R. J., Espley, J. R., Joergensen, P. S., et al. (2018). A new model of Jupiter's magnetic field from Juno's first nine orbits. *Geophysical Research Letters*, *45*, 2590–2596. <https://doi.org/10.1002/2018GL077312>

Cowley, S., & Bunce, E. (2003a). Modulation of Jovian middle magnetosphere currents and auroral precipitation by solar wind-induced compressions and expansions of the magnetosphere: Initial response and steady state. *Planetary and Space Science*, *51*(1), 31–56. [https://doi.org/10.1016/S0032-0633\(02\)00130-7](https://doi.org/10.1016/S0032-0633(02)00130-7)

Cowley, S., & Bunce, E. (2003b). Modulation of Jupiter's main auroral oval emissions by solar wind induced expansions and compressions of the magnetosphere. *Planetary and Space Science*, *51*(1), 57–79. [https://doi.org/10.1016/S0032-0633\(02\)00118-6](https://doi.org/10.1016/S0032-0633(02)00118-6)

Cravens, T. E., Howell, E., Waite, J. H., & Gladstone, G. R. (1995). Auroral oxygen precipitation at Jupiter. *Journal of Geophysical Research*, *100*(A9), 17153. <https://doi.org/10.1029/95ja00970>

Cravens, T. E., Waite, J. H., Gombosi, T. I., Lugaz, N., Gladstone, G. R., Mauk, B. H., & MacDowall, R. J. (2003). Implications of Jovian X-ray emission for magnetosphere-ionosphere coupling. *Journal of Geophysical Research*, *108*(A12), 1–12. <https://doi.org/10.1029/2003JA010050>

Delamere, P. A., & Bagenal, F. (2010). Solar wind interaction with Jupiter's magnetosphere. *Journal of Geophysical Research*, *115*, 1–20. <https://doi.org/10.1029/2010JA015347>

Desroche, M., Bagenal, F., Delamere, P. A., & Erkaev, N. (2012). Conditions at the expanded Jovian magnetopause and implications for the solar wind interaction. *Journal of Geophysical Research*, *117*, 1–18. <https://doi.org/10.1029/2012JA017621>

Dunn, W. R., Branduardi-Raymont, G., Elsner, R. F., Vogt, M. F., Lamy, L., Ford, P. G., et al. (2016). The impact of an ICME on the Jovian X-ray aurora. *Journal of Geophysical Research A: Space Physics*, *121*, 2274–2307. <https://doi.org/10.1002/2015JA021888>

Dunn, W. R., Branduardi-Raymont, G., Ray, L. C., Jackman, C. M., Kraft, R. P., Elsner, R. F., et al. (2017). The independent pulsations of Jupiter's northern and southern X-ray auroras. *Nature Astronomy*, *1*(11), 758–764. <https://doi.org/10.1038/s41550-017-0262-6>

Ebert, R. W., Allegrini, F., Bagenal, F., Bolton, S. J., Connerney, J. E. P., Clark, G., et al. (2017). Accelerated flows at Jupiter's magnetopause: Evidence for magnetic reconnection along the dawn flank. *Geophysical Research Letters*, *44*, 4401–4409. <https://doi.org/10.1002/2016GL072187>

Ebert, R. W., Allegrini, F., Bagenal, F., Bolton, S. J., Connerney, J. E. P., Clark, G., et al. (2017). Spatial distribution and properties of 0.1–100 electrons in Jupiter's polar auroral region. *Geophysical Research Letters*, *44*, 9199–9207. <https://doi.org/10.1002/2017GL075106>

Ebert, R. W., Bagenal, F., McComas, D. J., & Fowler, C. M. (2014). A survey of solar wind conditions at 5 AU: A tool for interpreting solar wind-magnetosphere interactions at Jupiter. *Frontiers in Astronomy and Space Sciences*, *1*, 1–13. <https://doi.org/10.3389/fspas.2014.00004>

Efron, B., & Stein, C. (1981). The jackknife estimate of variance. *The Annals of Statistics*, *9*(3), 586–596. <https://doi.org/10.1214/aos/1176345462>

Elsner, R. F., Lugaz, N., Waite, J. H., Cravens, T. E., Gladstone, G. R., Ford, P., et al. (2005). Simultaneous Chandra X ray Hubble Space Telescope ultraviolet, and Ulysses radio observations of Jupiter's aurora. *Journal of Geophysical Research*, *110*, 1–16. <https://doi.org/10.1029/2004JA010717>

Fuselier, S. A., Trattner, K. J., Petrinc, S. M., & Lavraud, B. (2012). Dayside magnetic topology at the Earth's magnetopause for northward IMF. *Journal of Geophysical Research*, *117*, 1–14. <https://doi.org/10.1029/2012JA017852>

Gladstone, G. R., Waite, J. H., Grodent, D., Lewis, W. S., Crary, F. J., Eisner, R. F., et al. (2002). A pulsating auroral X-ray hot spot on Jupiter. *Nature*, *415*, 1000–1003. <https://doi.org/10.1038/4151000a>

Gosling, J. T., Thomsen, M. F., Bame, S. J., Onsager, T. G., & Russell, C. T. (1990). The electron edge of low latitude boundary layer during accelerated flow events. *Geophysical Research Letters*, *17*, 1833–1836. <https://doi.org/10.1029/GL017i011p01833>

Grodent, D., Bonfond, B., Gérard, J. C., Radioti, A., Gustin, J., Clarke, J. T., et al. (2008). Auroral evidence of a localized magnetic anomaly in Jupiter's northern hemisphere. *Journal of Geophysical Research*, *113*, 1–10. <https://doi.org/10.1029/2008JA013185>

Guo, R. L., Yao, Z. H., Sergis, N., Wei, Y., Mitchell, D., Roussos, E., et al. (2018). Reconnection acceleration in Saturn's dayside magnetodisk: A multicase study with Cassini. *The Astrophysical Journal*, *868*(2), L23. <https://doi.org/10.3847/2041-8213/aaedab>

Hasegawa, H., Fujimoto, M., Phan, T.-D., Réme, H., Balogh, A., Dunlop, MW, et al. (2004). Transport of solar wind into Earth's magnetosphere through rolled-up Kelvin-Helmholtz vortices. *Nature*, *430*(7001), 755–758. <https://doi.org/10.1038/nature02799>

Hess, S. L. G., Bonfond, B., Zarka, P., & Grodent, D. (2011). Model of the Jovian magnetic field topology constrained by the Io auroral emissions. *Journal of Geophysical Research*, *116*, 1–19. <https://doi.org/10.1029/2010JA016262>

- Houston, S. J., Cravens, T. E., Schultz, D. R., Gharibnejad, H., Dunn, W. R., Haggerty, D. K., et al. (2019). Jovian auroral ion precipitation: X-ray production from oxygen and sulfur precipitation. *Journal of Geophysical Research: Space Physics*, *125*, e2019JA027007. <https://doi.org/10.1029/2019JA027007>
- Hui, Y., Schultz, D. R., Kharchenko, V. A., Bhardwaj, A., Branduardi-Raymont, G., Stancil, P. C., et al. (2010). Comparative analysis and variability of the Jovian X-ray spectra detected by the Chandra and XMM-Newton observatories. *Journal of Geophysical Research*, *115*, 1–19. <https://doi.org/10.1029/2009ja014854>
- Jackman, C. M., & Arridge, C. S. (2011). Solar cycle effects on the dynamics of Jupiter's and Saturn's magnetospheres. *Solar Physics*, *274*(1–2), 481–502. <https://doi.org/10.1007/s11207-011-9748-z>
- Jackman, C. M., Knigge, C., Altamirano, D., Gladstone, R., Dunn, W., Elsner, R., et al. (2018). Assessing Quasi-periodicities in Jovian X-ray emissions: Techniques and heritage survey. *Journal of Geophysical Research: Space Physics*, *123*, 9204–9221. <https://doi.org/10.1029/2018JA025490>
- Jansen, F., Lumb, D., Altieri, B., Clavel, J., Ehle, M., Erd, C., et al. (2001). XMM-Newton spacecraft and operations. *Astronomy and Astrophysics*, *365*, L1–L6. <https://doi.org/10.1051/0004-6361>
- Joy, S. P., Kivelson, M. G., Walker, R. J., Khurana, K. K., Russell, C. T., & Ogino, T. (2002). Probabilistic models of the Jovian magnetopause and bow shock locations. *Journal of Geophysical Research*, *107*(A10), 1–17. <https://doi.org/10.1029/2001JA009146>
- Khurana, K. K., & Kivelson, M. G. (1989). Ultralow frequency MHD waves in Jupiter's middle magnetosphere. *Journal of Geophysical Research*, *94*(A5), 5241. <https://doi.org/10.1029/ja094ia05p05241>
- Kimura, T., Kraft, R. P., Elsner, R. F., Branduardi-Raymont, G., Gladstone, G. R., Tao, C., et al. (2016). Jupiter's X-ray and EUV auroras monitored by Chandra, XMM-Newton, and Hisaki satellite. *Journal of Geophysical Research A: Space Physics*, *121*, 2308–2320. <https://doi.org/10.1002/2015JA021893>
- Krimigis, S. M., Mitchell, D. G., Hamilton, D. C., Dandouras, J., Armstrong, T. P., Bolton, S. J., et al. (2002). A nebula of gases from Io surrounding Jupiter. *Nature*, *415*(6875), 994–996. <https://doi.org/10.1038/415994a>
- Ma, X., Stauffer, B., Delamere, P. A., & Otto, A. (2015). Asymmetric Kelvin-Helmholtz propagation at Saturn's dayside magnetopause. *Journal of Geophysical Research: Space Physics*, *120*, 1867–1875. <https://doi.org/10.1002/2014JA020746>
- MacDowall, R. J., Kaiser, M. L., Desch, M. D., Farrell, W. M., Hess, R. A., & Stone, R. G. (1993). Quasiperiodic Jovian radio bursts: Observations from the Ulysses 1. MacDowall, R. J. et al. Quasiperiodic Jovian Radio bursts: Observations from the Ulysses radio and plasma wave experiment. *Planet. Space Sci.* *41*, 1059–1072 (1993). Radio and Plasma Wave Ex. *Planetary and Space Science*, *41*(11–12), 1059–1072. [https://doi.org/10.1016/0032-0633\(93\)90109-F](https://doi.org/10.1016/0032-0633(93)90109-F)
- Mann, I. R., Voronkov, I., Dunlop, M., Donovan, E., Yeoman, T. K., Milling, D. K., et al. (2002). Coordinated ground-based and Cluster observations of large amplitude global magnetospheric oscillations during a fast solar wind speed interval. *Annales Geophysicae*, *20*(4), 405–426. <https://doi.org/10.5194/angeo-20-405-2002>
- Manners, H., Masters, A., & Yates, J. N. (2018). Standing Alfvén waves in Jupiter's magnetosphere as a source of 10- to 60-min quasiperiodic pulsations. *Geophysical Research Letters*, *45*, 8746–8754. <https://doi.org/10.1029/2018GL078891>
- Mauk, B. H., Cohen, I. J., Haggerty, D. K., Hospodarsky, G. B., Connerney, J. E. P., Anderson, B. J., et al. (2019). Investigation of mass/charge-dependent escape of energetic ions across the magnetopauses of Earth and Jupiter (Vol. 124, pp. 5539–5567). <https://doi.org/10.1029/2019JA026626>
- Mauk, B. H., Haggerty, D. K., Jaskulek, S. E., Schlemm, C. E., Brown, L. E., Cooper, S. A., et al. (2017). The Jupiter Energetic Particle Detector Instrument (JEDI) investigation for the Juno mission. *Space Science Reviews*, *213*(1–4), 289–346. <https://doi.org/10.1007/s11214-013-0025-3>
- Maurellis, A. N., Cravens, T. E., Gladstone, G. R., Waite, J., Hunter, & Acton, L. W. (2000). Jovian X-ray emission from solar X-ray scattering. *Geophysical Research Letters*, *27*(9), 1339–1342. <https://doi.org/10.1029/1999GL010723>
- McComas, D. J., Alexander, N., Allegrini, F., Bagenal, F., Beebe, C., Clark, G., et al. (2017). The Jovian Auroral Distributions Experiment (JADE) on the Juno mission to Jupiter. *Space Science Reviews*, *213*(1–4), 547–643. <https://doi.org/10.1007/s11214-013-9990-9>
- McComas, D. J., & Bagenal, F. (2007). Jupiter: A fundamentally different magnetospheric interaction with the solar wind. *Geophysical Research Letters*, *34*, 1–5. <https://doi.org/10.1029/2007GL031078>
- Metzger, A. E., Gilman, D. A., Luthy, J. L., Hurley, K. C., Schnopper, H. W., Seward, F. D., & Sullivan, J. D. (1983). Detection of X-rays from Jupiter. *Journal of Geophysical Research*, *88*, 7731–7741. <https://doi.org/10.1029/JA088iA10p07731>
- Moore, K. M., Yadav, R. K., Kulowski, L., Cao, H., Bloxham, J., Connerney, J. E. P., et al. (2018). A complex dynamo inferred from the hemispheric dichotomy of Jupiter's magnetic field. *Nature*, *561*(7721), 76–78. <https://doi.org/10.1038/s41586-018-0468-5>
- Ozak, N., Schultz, D. R., Cravens, T. E., Kharchenko, V., & Hui, Y. W. (2010). Auroral X-ray emission at Jupiter: Depth effects. *Journal of Geophysical Research*, *115*, 1–13. <https://doi.org/10.1029/2010JA015635>
- Quenouille, M. H. (1949). Problems in plane sampling. *The Annals of Mathematical Statistics*, *20*(3), 355–375. <https://doi.org/10.1214/aoms/117729989>
- Quenouille, M. H. (1956). Notes on bias in estimation. *Biometrika*, *43*(3/4), 353. <https://doi.org/10.2307/2332914>
- Rae, I. J., Donovan, E. F., Mann, I. R., Fenrich, F. R., Watt, C. E. J., Milling, D. K., et al. (2005). Evolution and characteristics of global Pc5 ULF waves during a high solar wind speed interval. *Journal of Geophysical Research*, *110*, 1–16. <https://doi.org/10.1029/2005JA011007>
- Southwood, DJ, & Kivelson, MG (2001). A new perspective concerning the influence of the solar wind on the Jovian magnetosphere. *Journal of Geophysical Research*, *106*(1), 6123–6130. <https://doi.org/10.1029/2000JA000236>
- Vaughan, S. (2005). A simple test for periodic signals in red noise. *Astronomy and Astrophysics*, *431*(1), 391–403. <https://doi.org/10.1051/0004-6361:20041453>
- Vogt, M. F., Bunce, E. J., Kivelson, M. G., Khurana, K. K., Walker, R. J., Radioti, A., et al. (2015). Magnetosphere-ionosphere mapping at Jupiter: Quantifying the effects of using different internal field models. *Journal of Geophysical Research: Space Physics*, *120*, 2584–2599. <https://doi.org/10.1002/2014JA020729>
- Vogt, M. F., Gyalay, S., Kronberg, E. A., Bunce, E. J., Kurth, W. S., Zieger, B., & Tao, C. (2019). Solar wind interaction with Jupiter's magnetosphere: A statistical study of galileo in situ data and modeled upstream solar wind conditions. *Journal of Geophysical Research: Space Physics*, *124*, 10,170–10,199. <https://doi.org/10.1029/2019JA026950>
- Vogt, M. F., Kivelson, M. G., Khurana, K. K., Walker, R. J., Bonfond, B., Grodent, D., & Radioti, A. (2011). Improved mapping of Jupiter's auroral features to magnetospheric sources. *Journal of Geophysical Research*, *116*, A03220. <https://doi.org/10.1029/2010JA016148>
- Weisskopf, M. C., Tananbaum, H. D., Van Speybroeck, L. P., & O'Dell, S. L. (2000). Chandra X-ray observatory (CXO): Overview. *X-Ray Optics, Instruments, and Missions III*, *4012*, 2–16. <https://doi.org/10.1117/12.391545>

- Wilson, R. J., Delamere, P. A., Bagenal, F., & Masters, A. (2012). Kelvin-Helmholtz instability at Saturn's magnetopause: Cassini ion data analysis. *Journal of Geophysical Research*, *117*, A03212. <https://doi.org/10.1029/2011JA016723>
- Wilson, R. J., & Dougherty, M. K. (2000). Evidence provided by galileo of ultra low frequency waves within Jupiter's middle magnetosphere. *Geophysical Research Letters*, *27*(6), 835–838. <https://doi.org/10.1029/1999GL010750>
- Zhang, B., Delamere, P. A., Ma, X., Burkholder, B., Wiltberger, M., Lyon, J. G., et al. (2018). Asymmetric Kelvin-Helmholtz instability at Jupiter's magnetopause boundary: Implications for corotation-dominated systems. *Geophysical Research Letters*, *45*, 56–63. <https://doi.org/10.1002/2017GL076315>